MBE-GROWN InGaN EPILAYERS

A Thesis submitted to the Department of Physics

University of Strathclyde

For the Degree of Master of Philosophy

By

Isabel Fernández-Torrente

August 2003

ABSTRACT

Two main methods are used for $In_xGa_{1-x}N$ growth: high-temperature Metalorganic Chemical Vapour Deposition (MOCVD), proven to be successful for the growth of materials for commercial devices with low InN content ($x<0.3$), and low-temperature Molecular Beam Epitaxy (MBE), with better prospects for obtaining higher InN fractions ($x>0.5$). A direct comparison between MOCVD and MBE InGaN epilayers with similar InN concentration has been performed for the first time. The InN fraction in available MOCVD epilayers varies from 0 to 0.4 while in our MBE samples the range is 0.13-0.35. Wavelength Dispersive X-ray (WDX) analysis was performed to determine the composition of the samples. In-situ cathodoluminescence (CL) and ex-situ photoluminescence (PL) energy mapping were combined with large-area optical absorption spectroscopy in order to assess the optical properties of the materials. The composition dependencies of the optical energies are found to *vary with the growth method*. The trendline of PL/CL peak energy versus InN fraction is linear in both cases with comparable slopes but different intercepts for zero InN fraction. An "S-shape effect" of PL emission energy also appears with temperature, accompanied by an anomalous behaviour of the emission linewidth. We will try to explain these results.

ACKNOWLEDGEMENTS

In first place I want to thank my family, for all the support they give to me. Also many thanks to my supervisor, K.P. O'Donnell, for his help during the progress of this report, especially the writing, and R.W. Martin for providing me with the samples necessary to carry out this research.

Many thanks are due to other members of the group: Carol Trager-Cowan, the postdocs Paul Edwards and Stéphane Dalmasso and the other students: Frank Sweeney and his cups of tea, Yaroslav Feofanov, Debbie Amabile and Slava Katchkanov, colleagues at the office, and especially Raúl Pecharromán-Gallego, who is a great colleague and also a better friend.

Thanks to Dave Clark for fixing the vacuum and heating system whenever it was necessary. Regards are due to the "summer students", who stayed here only for a few months and to the good friends I have made during my stay in Glasgow.

TABLE OF CONTENTS

1. INTRODUCTION

1.1 SEMICONDUCTORS THAT EMIT LIGHT

1.1.1 Semiconductors

A semiconductor is a material whose electrical conductivity lies between those of metals and insulators [1]. We can make a first classification of these materials in two groups: elemental semiconductor materials, found in group IV of the periodic table, and compound semiconductor materials, formed from combinations of groups III and V or groups II and VI. These compounds can be binary, ternary or quaternary depending on the number of elements that are mixed: two, three or four respectively.

Examples of elemental semiconductor materials are Si and Ge, whose applications are known since the invention of the transistor in 1947 (using Ge) and its development in 1954 using Si [2]. As compound semiconductors we can enumerate ZnS, ZnSe, CdS, which are II-VI compounds, and AlN, InN, GaN, GaAs, GaP, as binary, InGaN, ternary, and AlGaInN, quaternary examples of III-V compounds. In this work we will study and analyse the properties of one important compound semiconductor: InGaN.

The interest in compound semiconductors with emission in the visible range is focused on their use for optical devices such as Light Emitting Diodes (LEDs) and Laser Diodes (LDs). While the first ones are used in traffic lights, graphics displays and room lightning (in the near future, with “white” LEDs) the features of blue/violet

LDs could improve the processing of data because of the smaller wavelength needed for reading the media: with smaller wavelengths and, as a result, smaller spots, it would be possible to store more data in less space as shown in the table of Figure 1.1. The High-Definition Digital Versatile Disc (HD-DVD) or Blu-ray Disc, whose marketing will compete with the actual DVD, has a capacity of around 30Gbytes of information. The laser used for reading/writing data in HD-DVDs is a blue one; GaN and InGaN are potential compounds for building these lasers [3]. The challenge the blue lasers have is related to writing: while the power requirements is 5mW continuous wave (CW) for reading, the writing function in this case requires a power in the 35-50mW range.

The material used for writing HD-DVDs should have a good performance, large power, low noise, good beam quality and low price, in order to have a good market expansion.

Optical Disc	CD →	DVD →	Blu-ray Disc
Data Storage Capacity	640MB	4.7GB	27GB
Video Recording	15 minutes for standard TV	2 hours for standard TV	2 hours for HDTV
Commercialization	1982~	1997~	2003~
Laserbeam Color	Infrared	Red	Violet
Wavelength	780nm	650nm	405nm
Device Material	GaAs	GaAs	GaN

Figure 1.1. Application of III-V compound semiconductors [4]

As was explained before, optical devices are based on either II-VI or III-V semiconductors. The first are based on ZnSe and the second on GaN. ZnSe and GaN emit at 440nm and 355nm, respectively, at low temperatures. In order to extend the

range of emission they have to be mixed with a third element: Cd in the case of II-VIs and In in the case of III-Vs.

At the beginning of the study of compound semiconductors the development of III-N semiconductors was very poor. Researchers focused on II-VI because of the advantage that they have a similar zincblende structure and almost the same lattice constant as GaAs, the material used as substrate. For III-N compounds it was impossible to find a lattice matched semiconductor substrate, which made the growth of III-N especially complicated.

One advantage III-N have over II-VI materials is that, despite the huge density of defects they have, III-N are efficient light emitters. Another advantage is the longer lifetime: II-VI are grown at lower temperatures than III-N but they are very fragile.

In short, III-N materials are intrinsically more stable, robust and efficient than II-VI compounds but the crystal growth is difficult due to the temperature conditions necessary and the lattice mismatch between substrates and active layers [5].

Talking about InGaN, one of the main problems it has, apart from the lack of a suitable substrate, is related to the growth technology. Indium is a very volatile material; as a result the In incorporation on the sample is improved by growth at lower temperatures. However, growth at low temperatures entails a loss in crystalline quality. In the next section the most popular growth techniques are described.

1.1.2 Growth of III-V compounds

Two main techniques are used for the growth of III-V compounds and, particularly, $In_xGa_{1-x}N$, where x indicates the InN content: Metalorganic Chemical Vapour Deposition (MOCVD)[1], proven to be succesful in the growth of materials with low InN content ($x < 0.3$), and Molecular Beam Epitaxy (MBE), with better prospects for higher InN fractions ($x > 0.5$).

MOCVD (MOVPE) Growth

MOCVD is used to prepare high purity semiconductors devices. MOCVD uses a chemical reaction between metal alkyl vapours (precursors) and non-metal hydride gases stored in separate containers to a hot and usually rotating substrate surface. Substrate rotation improves film uniformity.

A binary compound such as GaN can be grown using trimethyl-gallium (TMGa) as a metalorganic source of the gallium and ammonia (NH_3) to supply nitrogen. For the growth of InGaN it will be necessary to use, as well as TMGa and NH_3, trimethyl-indium (TMIn) as the metalorganic source of Indium [6,7].

The metalorganic materials are stored in "bubblers"; a basic sketch is shown in Figure 1.3. The vapour pressure of these sources determines the growth rate and quality: too low pressures make difficult the transport of the material to the deposition zone inside the reaction chamber. A commercial MOCVD growth reactor is shown in Figure 1.4.

[1] And Metalorganic Vapour Phase Epitaxy (MOVPE) For semiconductors these two techniques are the same.

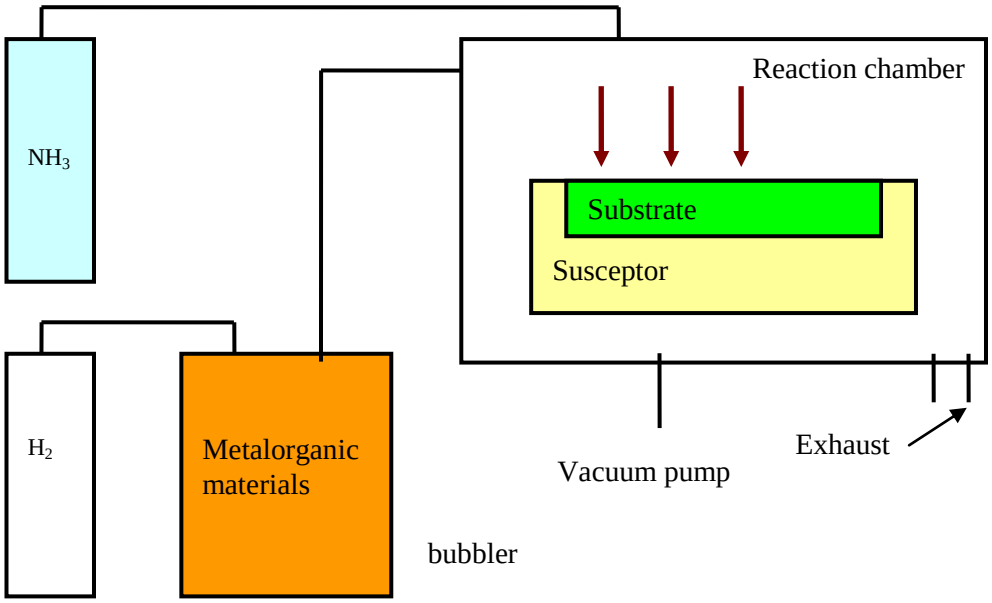

Figure 1.3. A typical MOCVD growth reactor system

In order to grow material, the metalorganic sources and hydrides are injected into the reactor chamber where they mix and transfer to the deposition area; in the deposition area the film precursors are formed by decomposition, at high temperatures, of sources and other gas-phase reactions. These precursors are useful for film growth: once they are transported to the growth surface and absorbed, atoms can incorporate into the growing film through surface reaction. The surplus products are sent away from the deposition zone towards the reaction exit (exhaust). A scheme of the growth reaction for GaN is shown in Figure 1.5.

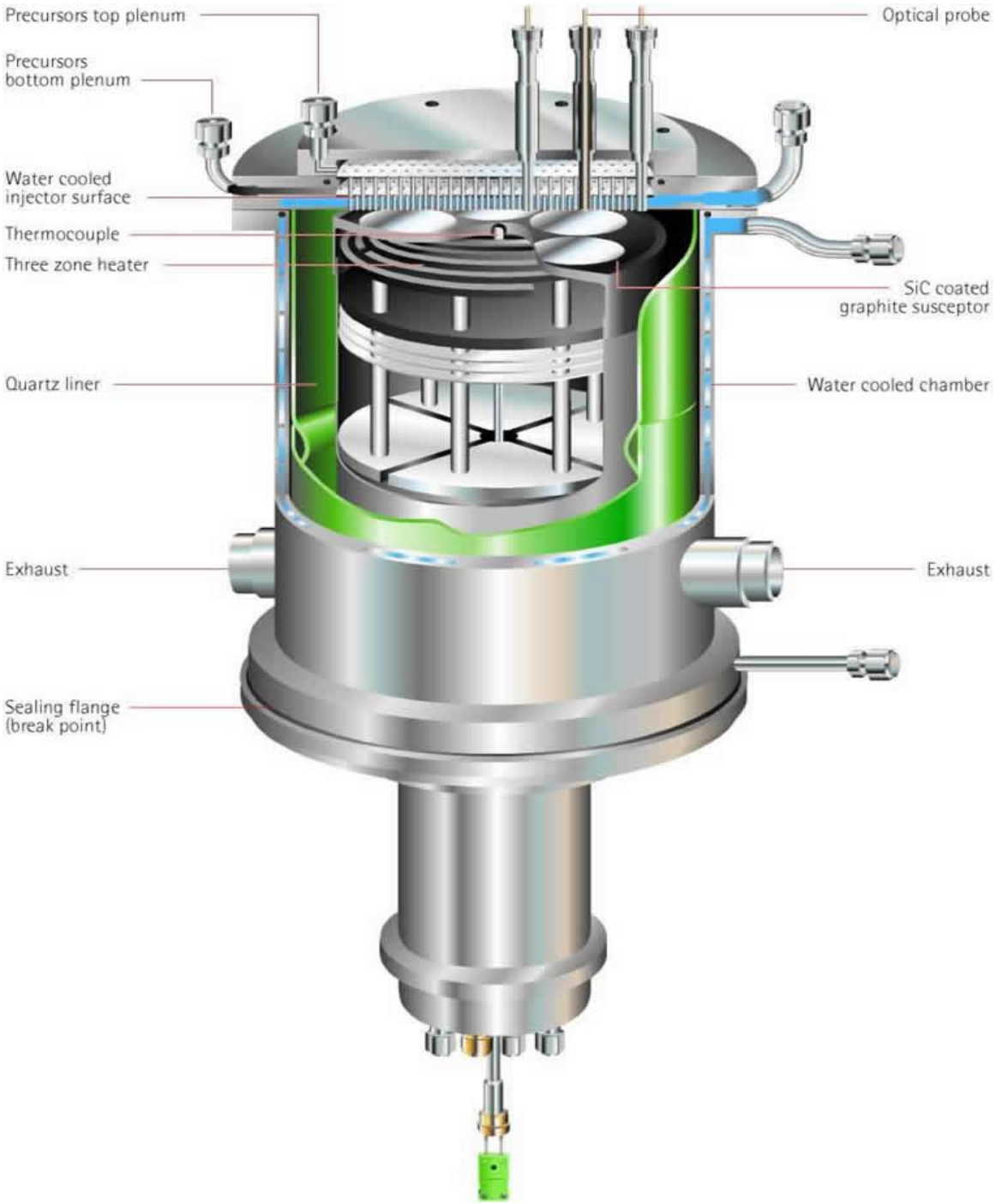

Figure 1.4. A commercial MOCVD growth reactor [8]

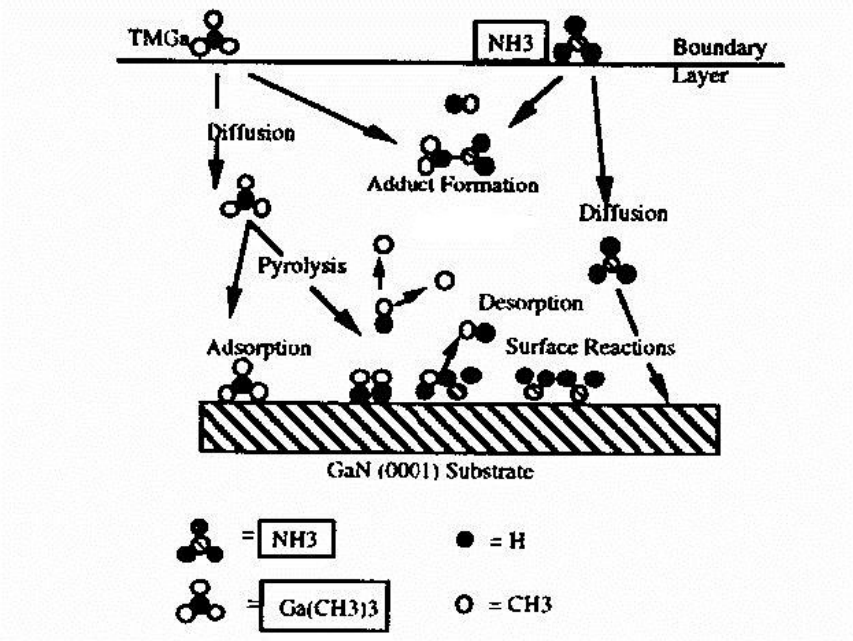

Figure 1.5. Reactions taking place during GaN growth [9]

One of the main problems of MOCVD growth is related to the low cracking efficiency of ammonia. For temperatures below 450ºC the cracking efficiency is nearly zero. Above this threshold the efficiency increases to reach a maximum of only 4% at 800ºC [10]. For that reason it is necessary to increase the ammonia flux in the reactor chamber, in order to maintain the right stoichiometry in the grown film. Usually a high amount of ammonia (nearly 50%) at high temperatures for enhancing thermal decomposition is required; physical properties of the ammonia will have an important effect on the flow dynamics of the reactor. Dimethylhydrazine (DMHy) has been used lately as an alternative nitrogen source; the disadvantage this compound presents is its high risk of explosion [3].

The need for high temperatures generates another problem related to MOCVD growth of InGaN with high InN concentration. Temperatures above 700°C are needed in order to grow InGaN with good crystalline quality; the disadvantage this range of temperatures has is the volatility of In, reported to be very high for temperatures close to 1000°C [3]. To be able to incorporate a high fraction of InN in the InGaN material the layers have to be grown at relatively lower temperatures and that is limiting the crystalline and optical quality (the emission would not be so efficient) [3]. Then a compromise between InN content and crystal quality is necessary when talking about MOCVD growth. Good quality layers are obtained for InN contents below 0.3.

Another main problem of InGaN growth is the lack of a suitable substrate. Even if GaN were available, InGaN would still be mismatched. The InGaN/GaN system is necessarily a "strained-layer" material.

MBE Growth

MBE was introduced in the early 1970s as a popular technique for the growth of III-V compounds [11]. Due to the low growth rate of the order of a few angstroms per second, MBE offers good control of layer thickness, doping, composition and growth of high quality layers with very abrupt interfaces.

MBE is the simplest epitaxial growth method: it is a refined form of ultrahigh vacuum (UHV) evaporation. In MBE the constituents of a semiconductor are deposited as molecular beams on top of a heated crystalline substrate to form thin epitaxial layers. The molecular beams typically originate from thermally evaporated

elemental sources, but other sources include metalorganic group III precursors, gaseous group V hydride or organic precursors may be used. For InGaN growth solid Gallium and Indium sources are used and ammonia or a nitrogen plasma as the nitrogen source [3]. A typical MBE growth reactor system is shown in Figure 1.6

Compared to MOCVD this technique has some advantages. The first one is that MBE does not require such high substrate temperatures: it is possible to grow InGaN samples with higher InN contents. Other advantages are the reduced contamination conditions due to the ultra-high vacuum (UHV) environment and high purity of sources, in-situ monitoring of surface reconstruction and growth environment, excellent layer thickness and interface control [12].

The main problems MBE growth has (in common with MOCVD) are the low cracking efficicency of ammonia and the lack of an appropriate substrate for the epitaxial growth fitting both the lattice parameter and the thermal expansion coefficient.

In order to resolve the first problem, nitrogen plasma may be used as nitrogen source. Although the first generation of nitrogen plasma-sources suffered from low growth rates and the presence of unwanted ionic species, it is possible now to grow high-quality GaN epilayers with growth rates larger than 1μm per hour [3]. Returning to the lack of an appropriate substrate: as a consequence of this, heteroepitaxy generates a high density of dislocations and defects on the layers. Although MOCVD is not free from these problems, the higher temperatures involved and the different kinetics generate much better results. Samples of $In_xGa_{1-x}N$ with x spanning the range $\sim 0.1<x<1$ have been produced by MBE.

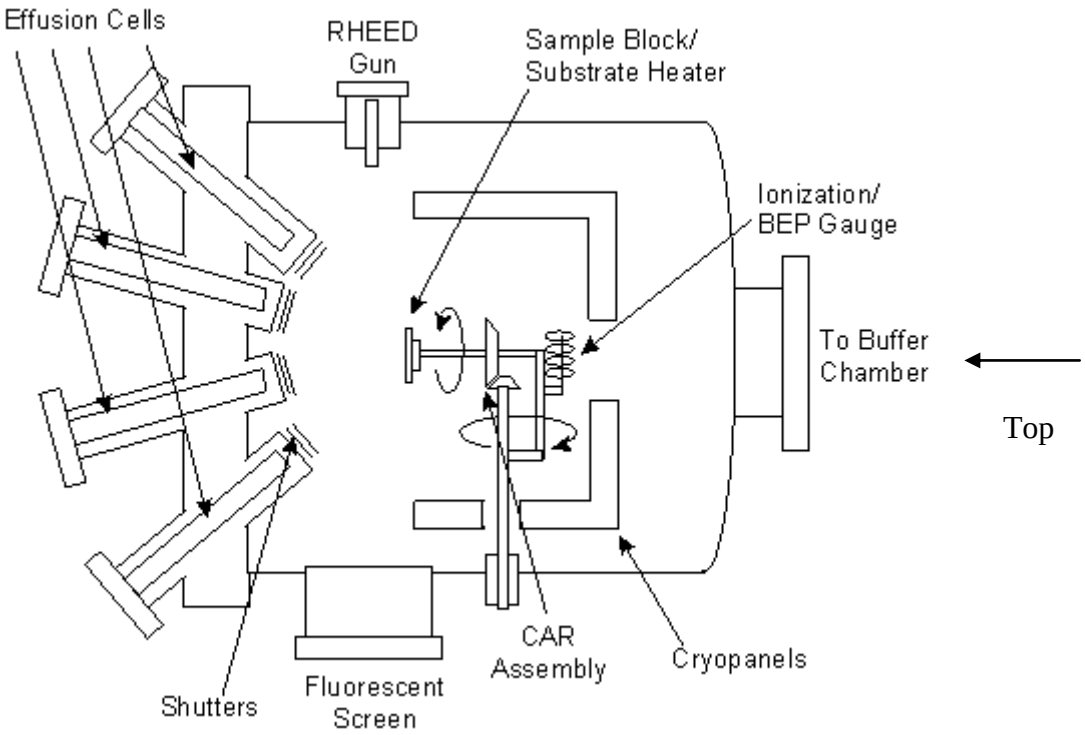

Figure 1.6. Typical MBE growth reactor system [13]

1.1.3 Samples

We have seen that MBE growth produces, due to the lower temperatures involved, samples with higher crystalline quality than MOCVD in the high InN content region.

Thus, we focused our study on two sets of samples that have been grown by MBE in the Departamento de Ingeniería Electrónica, Universidad Politécnica de Madrid, Spain [14]. The sample structures are shown in the schemes presented in Figure 1.7.

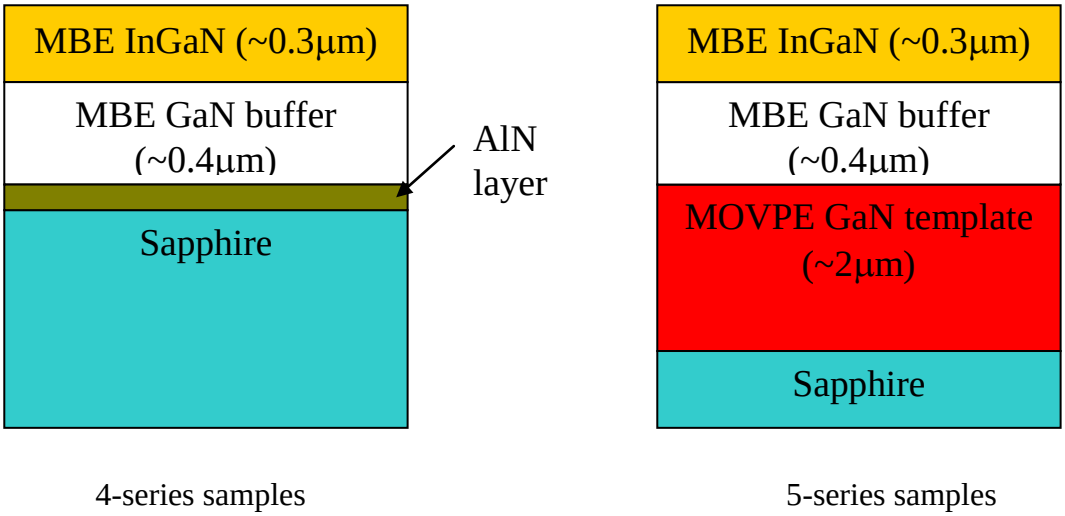

Figure 1.7. InGaN samples studied

Both sets of samples were grown using a MECA2000 MBE system; sapphire was used as a substrate. Although this material has some disadvantages as a substrate such as a very large lattice mismatch, reported to be around 16% for (0001) sapphire with GaN [15], and high thermal mismatch which generates a crystal growth with large quantity of defects, it has some other advantages that make it a good substrate; for example, low cost, availability, stability at high temperatures and transparency to visible light.

The use of a GaN buffer layer between the sapphire and the III-V material improves the quality of the material grown [16]; a nitridation of the sapphire surface ($Al_2O_3 \rightarrow AlN$) is generally carried out before growing this GaN buffer layer in order to improve its structural and optical properties [17]; the growth temperature of the GaN buffer layer also determines the structural quality of the InGaN epilayer. The material is improved a thin layer of GaN grown at low temperature is followed by a thick layer grown at high temperature.

Focusing on 4-series samples: a nitridation of the sapphire was first carried out. A small AlN layer, 10nm thick, was grown over this. Finally MBE GaN buffer layer was grown to allow, as we pointed out before, a better growth of the MBE InGaN layer.

The conditions for the growth of the last layer were changed from one sample to the other in the 4-series. During the growth of samples M479 and M481 In flux and growth temperature were kept constant ($2 \cdot 10^{-7}$Torr and 540ºC respectively), but the Ga flux was varied. Lower Ga fluxes produce higher InN concentration. In samples M480 and M485 both In flux and Ga flux were kept constant while growth temperature was varied [12]. Smaller InN concentrations are obtained with higher temperatures; this is due to increased In desorption at higher temperatures.

In the 5-series samples a MOVPE GaN template was grown on top of the sapphire and before the MBE GaN buffer layer. The use of such templates is expected to increase the quality of the active layer [18-20]. On top of this template the structure of 5-series is the same as in 4-series: a MBE GaN buffer layer followed by a MBE InGaN layer. The growth conditions for these epilayers are similar to samples M480 and M485: In and Ga fluxes are constant and temperatures vary from 500ºC to 600ºC.

A previous study of these samples has been carried out in 2002 by F.B. Naranjo et al [12,14,21]. Properties such as emission peak and width, energy bandgap and absorption band edge were measured. The results show a special behaviour of 5-series samples with temperature: multiple peak emission due to interference between bulk layers and air is found, a red-shift of luminescence followed by a blue shift at higher temperatures and also a minimum in the full width

at a half maximum (FWHM) depending on temperature. Minima of emission energy and FWHM take place at different temperatures.

The strain state and InN content of the samples were assessed by High Resolution X-ray Diffraction (HRXRD) and a bowing parameter of 3.6eV was calculated from optical absorption data assuming an InN bandgap of ~1.9eV.

In this report the optical properties of the samples described above will be measured and compared to the results obtained by Naranjo et al [12,14,21]. We will also compare the behaviour of these samples with InGaN epilayers grown by MOCVD, of great importance since MOCVD layers are the basis for commercial devices. The properties of these MOCVD samples, whose InN content varies between zero and 0.4, were measured in the same laboratory as measurements on the MBE samples were performed. Thus, a direct comparison between MOCVD and MBE InGaN epilayers can be performed. This investigation is the main aim of this report.

1.2 OPTICAL PROCESSES IN SEMICONDUCTORS

1.2.1 Electrons and holes in semiconductors

In the same way that an electron bound to an atom can only take discrete values of energy due to Pauli's principle, we can say that in a semiconductor the carriers are disposed in allowed energy bands separated by forbidden bands. Electrons occupy bands of allowed states.

Electrical processes in a semiconductor can be explained if two different forms of carrier are considered: electrons and holes, the last ones being positively charged "empty states" created when an electron leaves a band. The two carriers are complementary, holes are like bubbles in a liquid: liquid and bubbles move in opposite directions under gravity.

Conduction can only take place in a band that is partially empty. Electrons (holes) in a completely full band can only interchange states, but that means nothing in terms of conduction taking into account the fact that electrons (holes) are indistinguishable.

When an electron is locked in a chemical bond and is immobile it is said to be in the valence band. On gaining enough energy (thermal, electromagnetic field, etc) to break the bond and become a mobile carrier, this carrier is said to be promoted to the conduction band. The energy gap between the two allowed bands is called the energy bandgap, E_g, and its value (in eV) is a characteristic parameter of each semiconductor material. A scheme of the bands is shown in Figure 1.8.

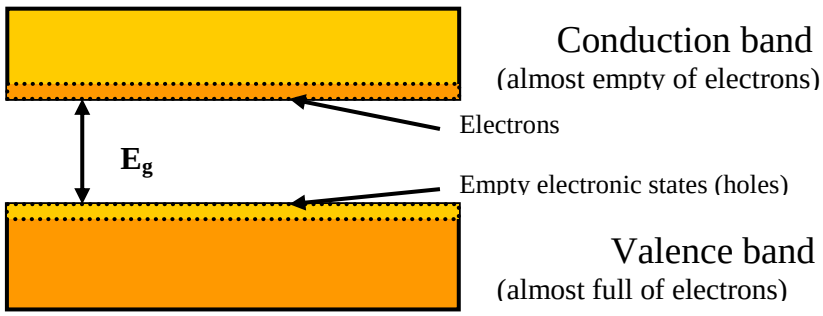

Figure 1.8. Semiconductor band structure diagram

Thus free carriers are produced when electrons travel from the valence band, normally almost filled with electrons, to the conduction band leaving holes in the valence band. Typical values of the bandgap energy are 1.1eV for Si and 3.4eV for GaN at room temperature [22].

1.2.2 Band structure of alloys

InGaN is a ternary compound consisting of some mixture of the binary compounds GaN and InN. Such a solid solution is called a semiconductor alloy. We can say that the composition of InGaN varies depending on the molar fractions of InN and GaN in the following way [23]:

$$In_xGa_{1-x}N = xInN + (1-x)\ GaN \qquad (1.1)$$

where x is the InN content of the alloy. Extending Vegard's law, which says that the lattice parameters of a substitutional solid solution is a weighted average of the values of the components, we can say that the properties of InGaN will be situated between those of InN and GaN.

GaN and InN have bandgaps reported to be 3.44eV [22] and 0.67eV [24] at room temperature and at 77 K respectively. Previous values of 1.89eV [22] reported for the InN bandgap at room temperature seem to be associated with layers of high carrier concentration [25].

Thus InGaN covers all the visible spectra from infrared (IR) to ultraviolet (UV); for emission in this range InGaN is found to be more efficient in the blue/UV region. Hence most studies of InGaN focus on the blue spectral region.

In theory x can reach values from x=0 (pure GaN) to x=1 (pure InN), but in practice high InN content values are not so easy to achieve because of the low solubility InN has in GaN. This fact causes problems while growing samples with high InN concentration and high crystal quality: it is quite difficult to have high-x samples that are homogeneous.

Previous studies of the variation of emission peak energy with InN content in the range $0 < x < 0.4$ for MOCVD-grown samples show that the peak emission energy depends, in that region, linearly on the InN concentration [26,27]. Due to the existing difficulties on the growth of MBE samples with low InN content and MOCVD samples with high InN content a study of the dependence of emission energy on InN content for samples grown in the same way and in the whole range from $x = 0$ to $x = 1$ has not yet been carried out. The only study which takes in the whole range $0<x<1$ combines results from MBE- and MOCVD-grown InGaN epilayers [28].

As well as the emission peak energy, the bandgap of InGaN varies with the InN concentration in the following way [29]:

$$E_g(x) = (1-x)\,E_g(GaN) + xE_g(InN) - bS_{xx} \quad (1.2)$$

Where E_g (GaN), E_g (InN) are the bandgap values for GaN and InN respectively and x is the InN content. The term S_{xx} is associated with the correlation function of the InN content at different spatial points of the material:

$$S_{xx} \sim \langle \Delta x(r)\, \Delta x(r') \rangle \quad (1.3)$$

Where r and r' are two points in the sample. Thus, this parameter, which is a perturbation term, depends on the way InN is distributed in the alloy. Assuming that the alloy is an ideal solution with random distribution of InN we can use the following simplification:

$$S_{xx} \sim x\,(1-x) \quad (1.4)$$

If we apply this approximation the bandgap of the InGaN alloy will depend on InN concentration in the following way:

$$E_g(x) = (1-x)\,E_g(GaN) + xE_g(InN) - b\,x\,(1-x) \quad (1.5)$$

The parameter b is known as the bowing parameter. A wide range of values for b has been reported from 1.0eV [30] to 3.2eV [31], but the value obtained by curve fitting depends strongly on the assumed InN bandgap. The values reported have been obtained assuming a value for InN bandgap of ~1.9eV.

It is also known that the emission peaks do not coincide with the bandgap energies. Due to relaxation of the exciton via phonon emission and percolation, the energy of the photon emitted is lower than the energy necessary to create the exciton. This difference between the emission peak and bandgap energy is known as Stokes' shift. Since the trendlines of both emission peak and bandgap energies tend to the same value for zero InN content it is expected for the Stokes' shift to decrease with the InN content on the epilayer reaching the theoretical value of zero for pure GaN.

1.2.3 A model for emission in semiconductors

The optical properties of a semiconductor are due to the processes that take place in the semiconductor associated with the absorption/emission of photons whose wavelength is situated in the appropriate spectral region. When talking about optics it is necessary to mention the exciton. An exciton is a particle formed by an electron and a hole whose motion is correlated by an attractive force (Coulomb force) between them. Electron and hole move in the exciton like the electron and proton in the hydrogen atom: thus we have bound states and continuum states of the exciton.

Excitons are created when the thermal equilibrium concentration of electron-hole pairs is changed by phenomena such as increase of temperature, absorption of photons or incidence of high-energy electrons on the semiconductor. In this non-equilibrium situation excess electrons and holes tend to relax towards quasi-thermal equilibrium distributions before recombining. The recombination is radiative if we have photon emission or it can be nonradiative if the energy of the electron-hole pair is dissipated in some other way, such as heat via excitation of phonons. These two

processes compete. A scheme of these two possible recombinations is shown in Figure 1.9, in a three level model.

An efficient luminescence material is one in which radiative transitions, B→A, predominate over non-radiative ones, C→A. Thus, the prescription for efficient light emitters is to help the radiative side of the competition that is intrinsic to the material by eliminating or at least reducing the processes that cause non-radiative decays.

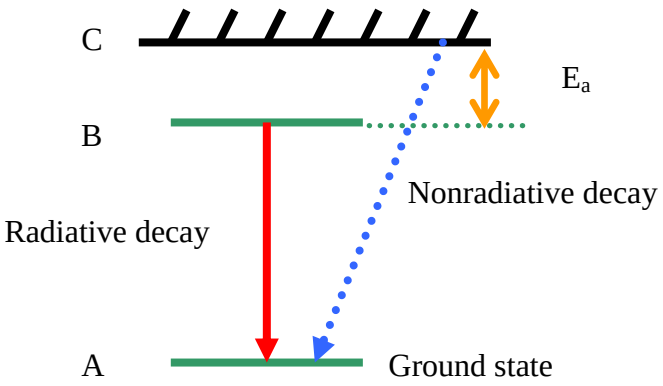

Figure 1.9. Three level model for radiative and nonradiative decays

The conditions for increasing the rate of radiative recombinations are first, a direct bandgap and second, a material with a low density of defects.

In a direct bandgap material valence band (VB) maximum and conduction band (CB) minimum both occur at the same k-value (k being the momentum in k-space diagrams). Transitions between the two allowed bands can take place with no change in crystal momentum. It is not necessary to have a third particle (phonon) with the appropriate momentum in order to satisfy the momentum conservation law

as happens with indirect bandgap materials, that are really much less efficient in the emission of light than direct bandgap materials.

Defects and impurities play an important role in recombination features: deep traps can create allowed states within the forbidden bandgap and electrons may transit from the conduction band to the valence band via the intermediate deep trap state without emitting any photon. In other cases defects can generate strains and electromagnetic fields. In this case the bands are shifted and excitons can decay in a nonradiative way.

Following the scheme presented in Figure 1.9 it is possible to say that an excited electron decays from B to A and generates a photon. At higher temperatures the electron can be thermally excited to the state C, in reality a band of states, from which the subsequent recombination is nonradiative. The threshold energy separating these two states, B and C, is called the activation energy (E_a). The higher the temperature the higher the population in C relative to B. Thus, a decrease of the photon emission is expected with increasing temperature.

The probability of having a radiative decay, that is, the emission efficiency, is:

$$\eta = \frac{N_B}{N_B + N_C} \tag{1.6}$$

Where N_B and N_C are the carrier populations of the radiative and nonradiative states in the three level model presented in Figure 1.9. The total number of carriers, N_B + N_C is constant with temperature. This ratio of populations assumes a Maxwell-Boltzmann distribution:

$$\frac{N_C}{N_B} = De^{\frac{-E_a}{kT}} \tag{1.7}$$

where D is a constant related to the degeneracy of available states on the band C and to the process rate, k is Boltzmann's constant and E_a is the activation energy we mentioned before. The emission efficiency can also be expressed in terms of the emitted intensity:

$$\eta = \frac{I}{I_0} \tag{1.8}$$

where I_0 and I are the photoluminescence intensity at temperature T=0 and T respectively.

By replacing equations (1.7) and (1.8) in (1.6) we obtain the following equation for the temperature dependence of the luminescence intensity:

$$I = \frac{I_0}{1 + De^{\frac{-E_a}{kT}}} \tag{1.9}$$

D is sometimes a function of temperature. In more detailed fits as, for example, Ashkinadze's model of exciton evaporation [32], the parameter D, as a ratio between band and impurity populations, would depend on the temperature as $D \sim T^{3/2}$.

We can see if we analyse equation (1.7) that an increase in temperature involves an increase in the population of carriers in the nonradiative band. This

would explain the decrease of luminous efficiency of the device with temperature. Temperature has also influence over the emission peak: it can change the emission energy and the width of the peak obtained. Both of these are expected to vary with the number of phonons that are excited at a given temperature. Usually peaks shift to lower energy and broaden with increasing temperature.

2. EXPERIMENTAL TECHNIQUES

In this report we will describe various kinds of experiments performed on MBE-grown InGaN epilayers that have been described in the first chapter. Optical absorption, photoluminescence (PL) and cathodoluminescence (CL) spectroscopies will be carried out in order to determine their optical energies. Absorption measurements will measure the bandgaps of the samples and the broadening of the band edge. PL and CL will provide information on the emission energies of the samples. We will study their composition with wavelength dispersive X-ray spectroscopy (WDX). The aim of these experiments is to establish the composition dependence of the optical energies. In addition the PL temperature dependence will compare radiative and non-radiative recombination.

2.1 ABSORPTION SPECTROSCOPY

Optical absorption is used to determine the band structure of semiconductors. By illuminating a semiconductor sample with light and measuring the variation of transmitted light with photon energy we determine at what energy transitions of the carriers take place.

The absorption set-up is shown in Figure 2.1. A tungsten lamp is used as a broad band light source. This light is introduced into a Bentham TM300 monochromator, with aperture f/4.1; a chopper located just before the slits of the monochromator modulates the focused light beam with a frequency of 30Hz, approximately.

In the monochromator a reflective diffraction grating splits the white light coming from the lamp in the extended visible spectrum (300-1000nm). A motor stepper, connected to a drive unit, moves the grating in order to select the output wavelength of the monochromator. This light is passed through the sample (situated in the sample holder shown in Figure 2.1) and the transmitted intensity is measured with a Hamamatsu R636 photomultiplier. The current signal from the photomultiplier is sent to a Stanford SR570 current preamplifier which converts it to a voltage signal. The output chopped DC voltage is sent afterwards to a Stanford SR810 DSP lock-in amplifier, in order to distinguish PL emission from background noise.

The lock-in amplifier is a phase-sensitive device: both excitation and luminescence signal have, taking into account that the lifetimes for the luminescence processes are small enough and they are not generating a big delay, approximately the same shape (because of the chopper). These two signals, excitation and luminescence are then in phase and their product is always a positive number. Any signal with different frequency and phase, such as noise whose variation is random, is removed by the lock-in. Finally, the digital DC output data of the lock-in amplifier are stored in a computer and analysed with an in-house program.

Thus, the spectra obtained in the computer correspond to the transmitted intensity obtained when the monochromatic light is passed through the sample as it is shown in Figure 2.2.

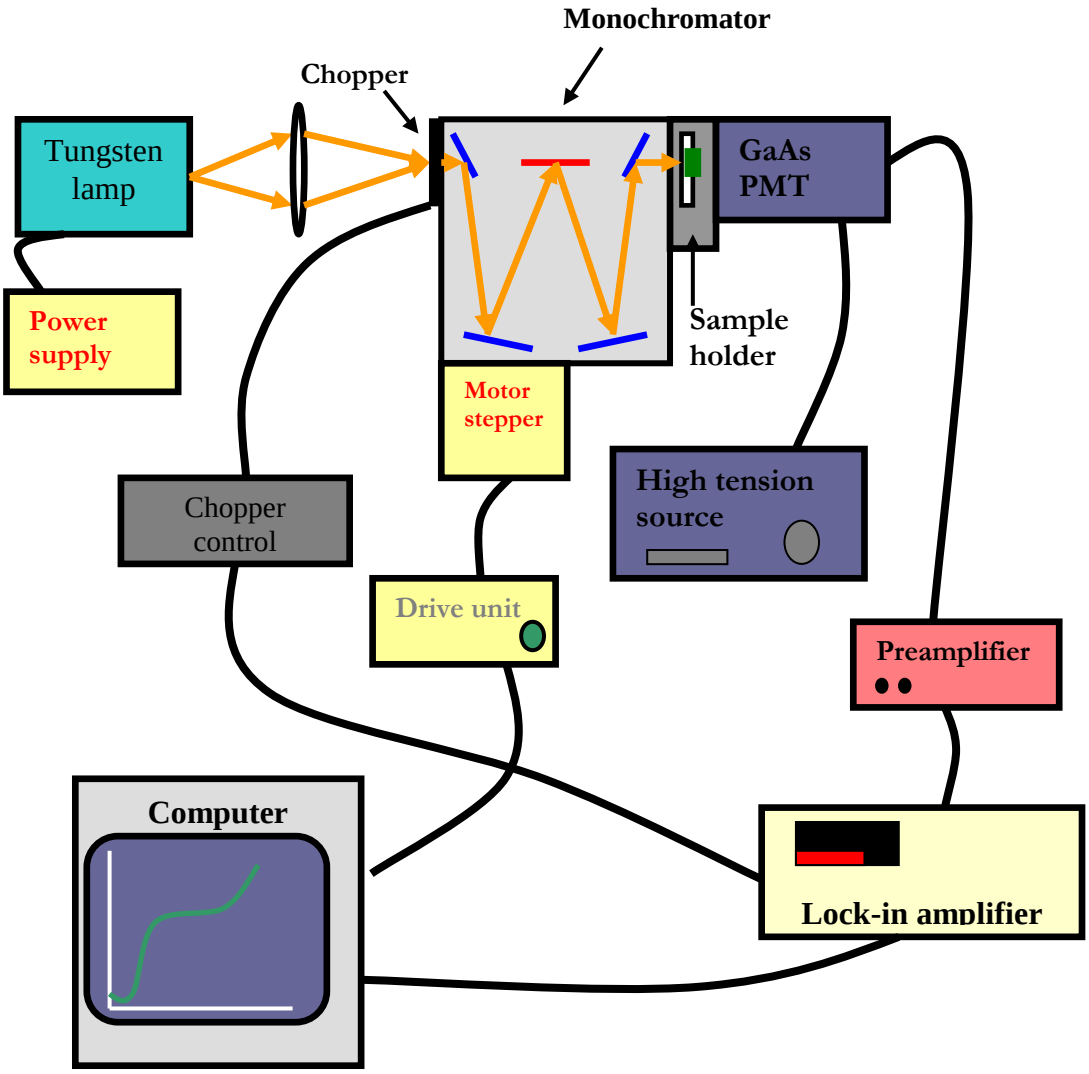

Figure 2.1. Absorption spectroscopy set up

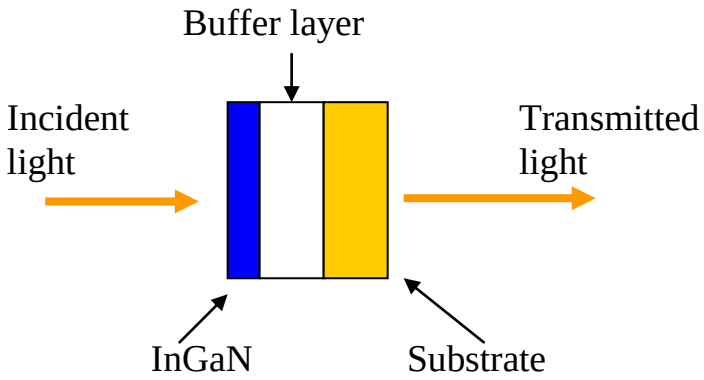

Figure 2.2. Absorption spectroscopy measurement

The transmitted light intensity depends on the sample thickness, its absorption coefficient α and on the photon energy (E) of the incident light.

$$I_t = I_0 e^{-\alpha(E)x} \tag{2.1}$$

Where I_t is the transmitted intensity, I_0 is the incident intensity coming from the light source, measured in the same set up without the sample in the sample holder, and x is the thickness of the sample. The value of the absorption coefficient can be deduced from equation (2.1). It is described by:

$$\alpha(E) = \frac{1}{x} Ln\left(\frac{I_0}{I_t}\right) \tag{2.2}$$

When the energy of the incident light is less than the gap energy photons are not absorbed strongly in the material but when this energy is approaching that of the bandgap the amount of absorbed light increases dramatically.

According to simple theory, this increase in the absorption (then also in the absorption coefficient) should be abrupt when the energy of the incident photons exceeds the energy bandgap E_b. In practice the change before and after the energy bandgap is smoother. The increase of the absorptance with the energy behaves in two ways near E_b: first an exponential increase with the energy is observed. This regime is known as the Urbach tail; its origin is the exponential tail of the density of states of

localised levels in the gap. Above this Urbach tail follows the absorption via transitions into extended states, which approximately follows an $E^{1/2}$ law.

A working definition of the absorption edge is proposed in [33] and can be used as an accurate description of the behaviour of the absorption coefficient close to the bandgap energy. This definition considers the effects of broadening and is provided by fitting the experimental curve, from the rising edge to the plateau, to the following sigmoidal formula:

$$\alpha(E) = \frac{\alpha_0}{1 + e^{\frac{E_b - E}{\Delta E}}} \tag{2.3}$$

Where E_b is the effective optical bandgap and ΔE the broadening of the absorption edge, equivalent to the Urbach tailing energy.

2.2 PHOTOLUMINESCENCE AND CATHODOLUMINESCENCE SPECTROSCOPIES

By luminescence we mean the light emitted by a body, excluding the thermal equilibrium black body radiation. For a semiconductor this process usually occurs when we have excess electrons and holes created by an excitation source. The recombination of electrons and holes entails the emission of a photon.

When the excitation source is light produced by a laser or a lamp the process of excitation of electrons and radiative recombination is called photoluminescence

(PL). Cathodoluminescence (CL) occurs when the excitation is produced by an electron beam. CL measurements were carried out at room temperature in the EPMA that will be described in paragraph 2.3.

The set up used for the PL measurements is shown in Figure 2.3. An Omnichrome 5mW He-Cd laser with UV output at 325nm is used as an excitation source. The laser light is introduced in an infinity-corrected microscope having in the entrance a band-pass filter for removing plasma lines from the discharge. Inside the microscope a dichroic mirror directs the laser line to the focusing system. The sample is brought into focus by moving the sample holder in the vertical direction (z). A x-y stage allows different regions to be excited.

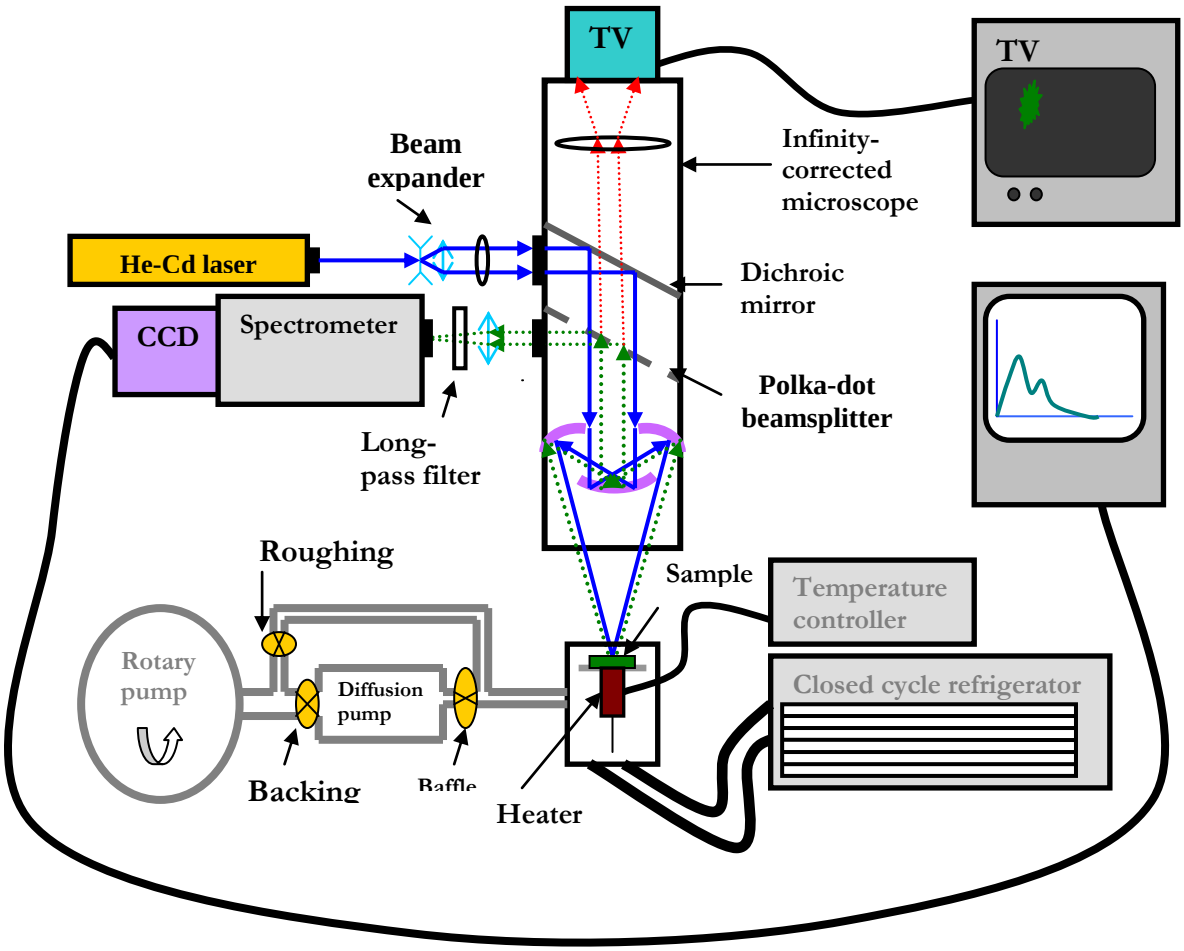

Figure 2.3. Photoluminescence set up

The luminescence emitted from the sample is collected in the same microscope: a polka-dot beam splitter (50% mirror, 50% quartz) splits up the luminescence in two beams. The first one enters the detection system consisting of a Oriel MultiSpec spectrometer and a cooled CCD camera and the second one goes to a TV camera, where the image obtained is used for focusing the sample and selecting the excited region.

The CCD camera is connected to a computer where the data are stored. The program used to visualise the spectra obtained is commercial software provided by the CCD manufacturer, Andor Technology.

The holder containing the sample is mounted in a vacuum chamber, inside a cryostat. With the help of a temperature controller (Oxford Intelligent Temperature Controller ITC 4) and a heater (the resistor), the sample temperature can be controlled in the range from approximately 10K to 300K.

2.3 WAVELENGTH-DISPERSIVE X-RAY SPECTROSCOPY

Wavelength dispersive X-ray spectroscopy (WDX) has proven to be a useful tool for determining the composition of solid samples studied [33-35]. In WDX a focused electron beam hits the sample; a small portion of the X-rays generated enters an X-ray spectrometer and impinges on an analysing crystal which causes the diffraction of the X-rays; they are diffracted according to Bragg's law:

$$n\lambda = 2d \sin\theta \qquad (2.4)$$

Where n is an integer, λ is the X-ray wavelength, d is the interplanar distance of the analysing crystal and θ is the angle of incidence of the X-ray beam over the crystal. A gas-filled proportional counter detects these scattered rays. Subsequently an analysis of X-ray intensity as a function of crystal angle is performed, by comparing the results with well known standards, in order to associate the position and intensity of the peaks observed with the amount of each element in the sample.

The advantages that EPMA-WDX has over Energy Dispersive Spectroscopy (EDS) are, among others, a better spectral resolution (the peaks do not overlap), much reduced background, less dead time in the data-collection process and a minimum number of spectral artifacts of the type that cause peak positions shifts or incorrect elemental assignments. Whereas EDS is semi-quantitative, at best, WDX aspires to accurate quantitative measurements [34,35].

The WDX measurements were taken in a Cameca SX100 Electron Probe Microanalyser (EPMA) shown in Figure 2.4. EPMA is basically a method of non-destructive elemental analysis of micron-sized volumes. A focused electron beam bombards a micro-volume of a sample with energy in the range 0kV to 50kV. The larger the energy of the beam, the greater the penetration of this beam into the sample. The sample is located on a stage allowing movement in the three spatial directions (X, Y and focus Z) controlled by the computer with accuracy of the order of 1μm.

The Strathclyde EPMA has three WDX spectrometers and a EDS detector in parallel; each spectrometer has two or four diffracting crystals in order to measure the X-ray emission spectrum from the sample. The appropriate crystals must be selected depending on the elements expected. For InGaN, for instance, three crystals

are selected in order to measure In, N and Ga. These are LPET (large pentaerythritol), PC1 (a synthetic pseudocrystal) and TAP (thallium acid phthalate) respectively. Quantitative analysis involve the use of certified standard reference materials, known as calibration standards, in order to perform the instrumental calibration. In the case of InGaN essays, InP and GaN were used as calibration standards.

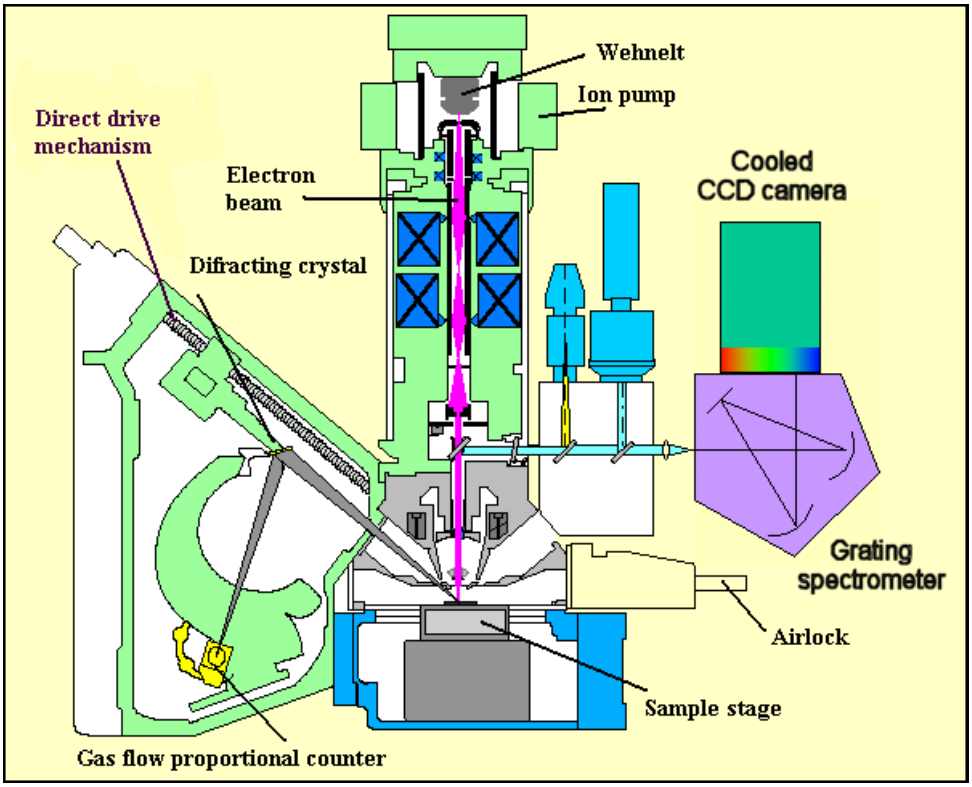

Figure 2.4. Cameca SX100 Electron probe microanalyser [35]

3. EXPERIMENTAL RESULTS

In this chapter we present the results obtained in wavelength-dispersive X-ray (WDX), photoluminescence (PL), cathodoluminescence (CL) and optical absorption spectroscopies of MBE-grown InGaN samples.

3.1 InN CONTENT OF InGaN SAMPLES

WDX measurements were carried out in order to determine the InN content of every sample [36]. Bulk analyses of the InGaN layer were performed in the EPMA using a focused electron beam with energies ranging from 5kV to 12kV and a beam current of the order of 10nA, low enough to avoid damage to the sample. Three different diffracting crystals were used in order to determine the atomic proportion of every element of interest (In, Ga and N) in the epilayer. The different beam voltages used allow us to measure any dependence of the InN content on the depth. The Grünn penetration range estimates, as a function of the energy of the beam, the depth at which 90% of incident electrons are absorbed in the material [37]:

$$R_G = \frac{3.98 \cdot 10^{-2}}{\rho} E_0^{1.75} \qquad (3.1)$$

where ρ is the density of the material (InGaN in this case) and E_0 is the energy of the beam. A beam voltage of 5kV would produce a Grünn penetration range of, approximately, 100nm while the 12kV beam would penetrate into the material to a depth of 500nm. The InGaN layers have a nominal thickness of 300nm. The InN contents measured with various beam energies are plotted in Figure 3.1.

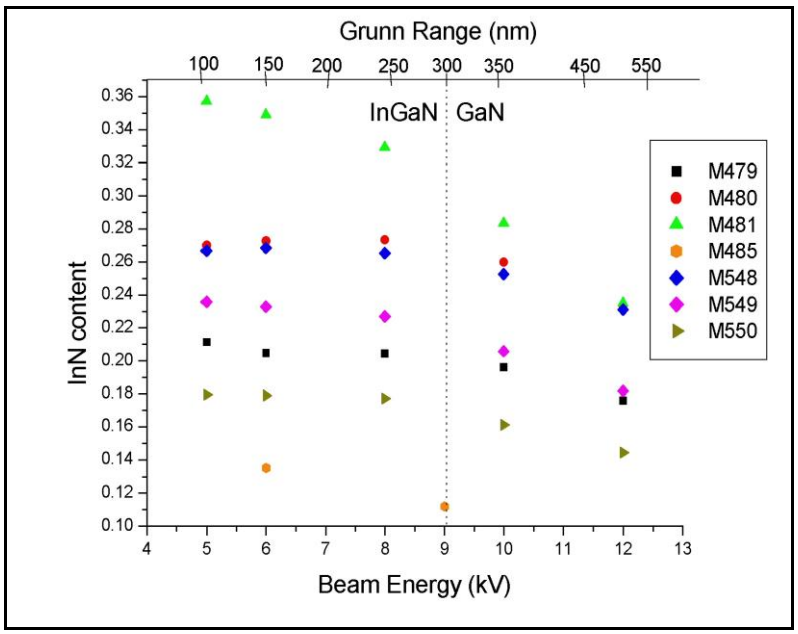

Figure 3.1. InN variation with beam energy

We can see that, up to 8 kV, the InN content remains constant for all samples except for M481 and M485, where the value drops continually with beam energy. The best estimate of the mean InN content of each sample (at 6kV) is shown in Table 3.1.

Sample	InN content (%)
M548	26.8 (2)
M549	23.3 (1)
M550	17.9 (2)
M479	20.5 (3)
M480	27.3 (6)
M481	34.9 (2)
M485	13.5 (2)

Table 3.1. InN fractions of InGaN epilayers

3.2 LOW TEMPERATURE PL MAPPING

Prior to detailed investigation a PL mapping of the samples was carried out in order to study the homogeneity of luminescence in the different InGaN epilayers. Spectra were taken at a temperature of 16K at regular spatial intervals of 0.5mm in a 2 dimensional array in the central part of each sample. The PL set up shown in the last chapter, Figure 2.3, was used. The maps are generated by plotting the PL emission peak energy as a function of the spatial variables X, Y. A gaussian fit was used in the computer package Origin 6.0 to estimate the position of the emission peak at every point. Example fits are shown in Figures 3.2 (a)-(b). The equation for the fit is the following one:

$$y = a\exp\left\{\frac{-(x-b)^2}{w^2}\right\} \tag{3.2}$$

where a is the amplitude of the PL peak (arbitrary units), x the emission energy at which the intensity, stored as variable y, is recorded and w is a broadening parameter related to the full width at half maximum (FWHM) as shown in equation (3.2):

$$FWHM = w\sqrt{2Ln(2)} \tag{3.3}$$

The fitting error in the peak position is smaller in 4-series samples than in the 5-series because of their more regular spectral shapes. The 2 dimensional maps obtained are shown in Figures 3.3 (a)-(g). In these maps we can see that the difference between the maximum and the minimum emission energy for a given sample lies between ~30meV and 60meV. Such an energy range implies variations in

InN content of around 1% - 2%. These variations are also spatially regular in one direction except in sample M548, where a scratch in the surface was found.

We can conclude, taking into account that the lowest InN content is 13.5% and the diameter of the laser spot for PL is of the order 10μm, that the samples are homogeneous enough, within the limits of accuracy, for the PL and absorption measurements we want to do.

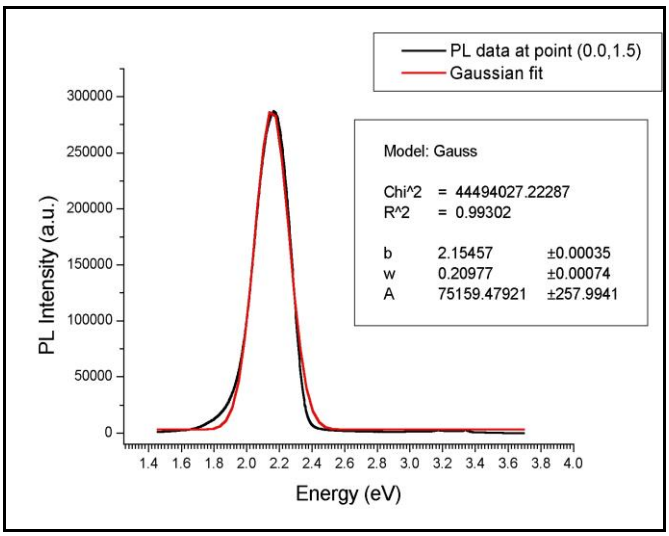

Figure 3.2(a). Gaussian fit to a PL spectrum of Sample M480

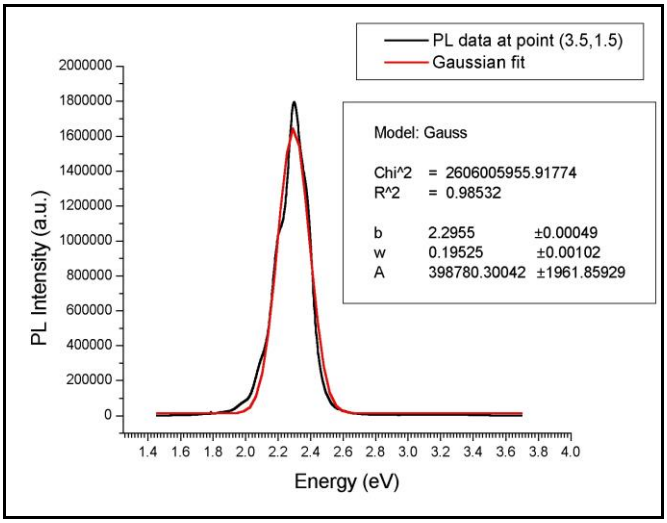

Figure 3.2(b). Gaussian fit to a PL spectrum of Sample M549

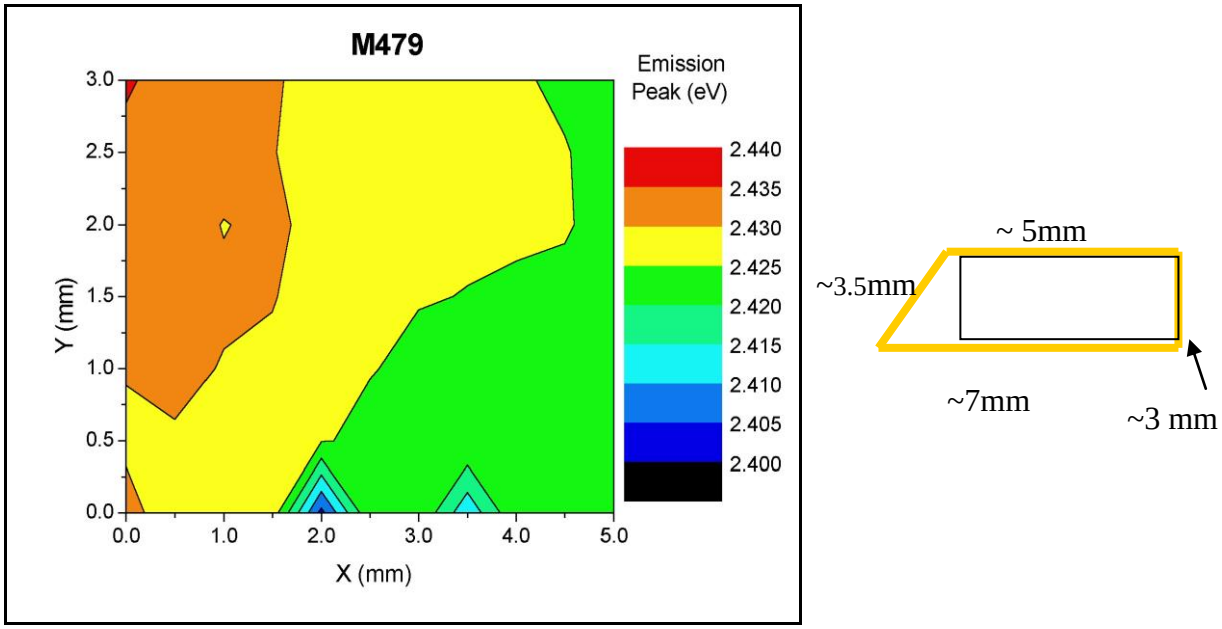

Figure 3.3 (a)

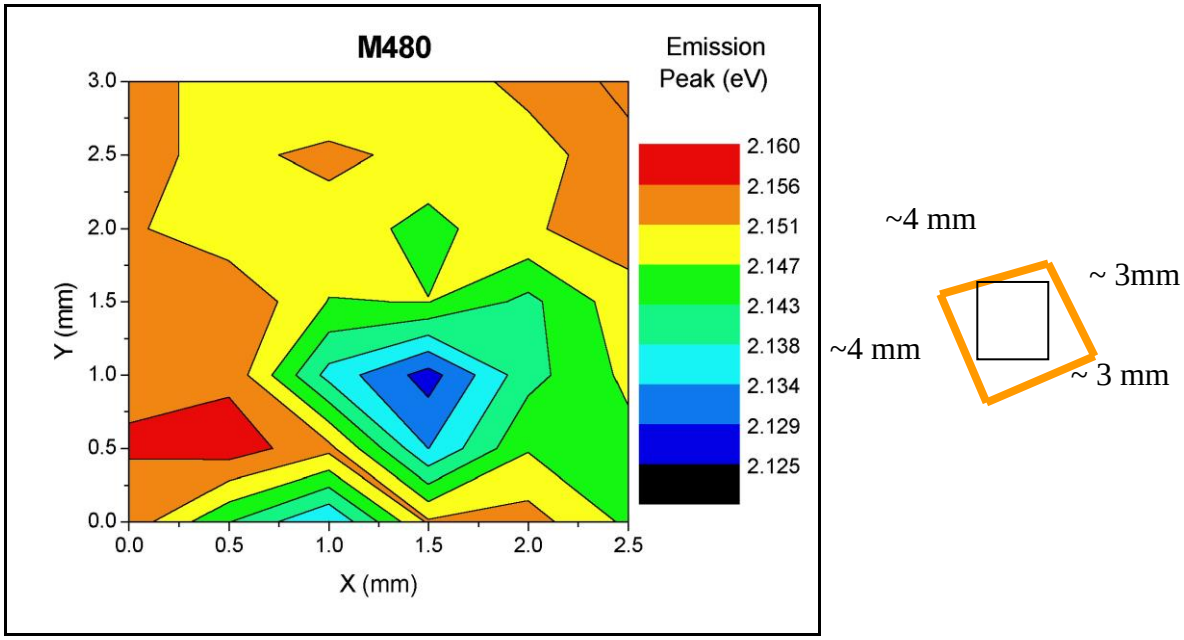

Figure 3.3 (b)

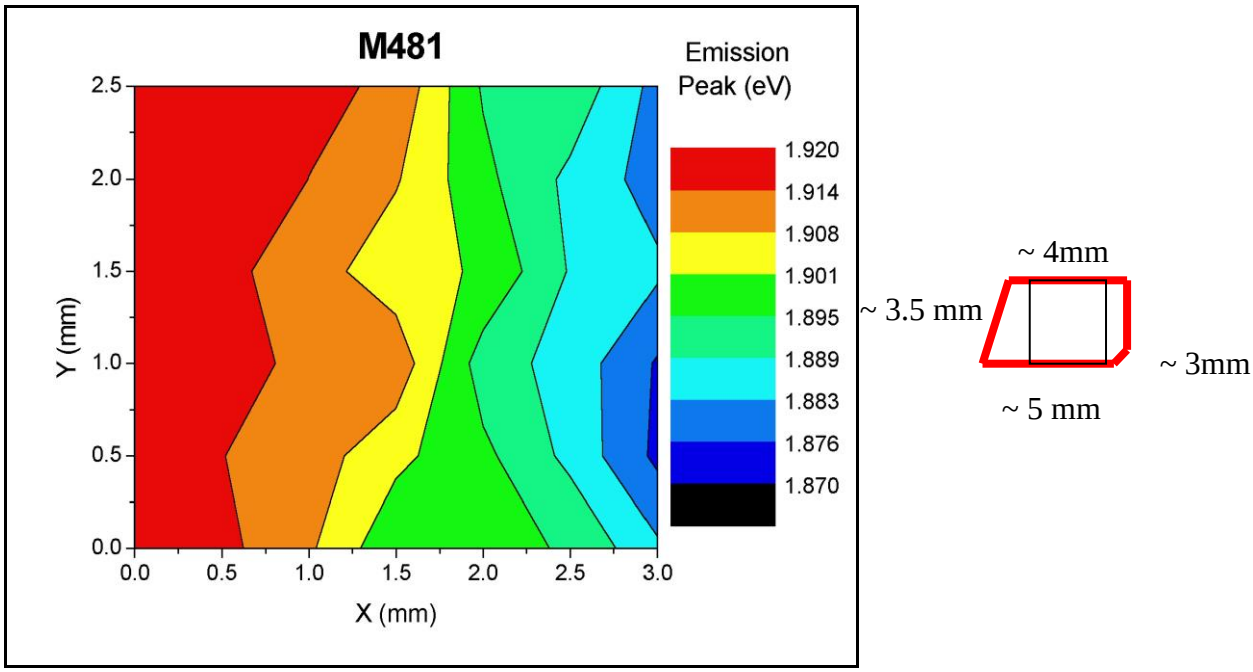

Figure 3.3 (c)

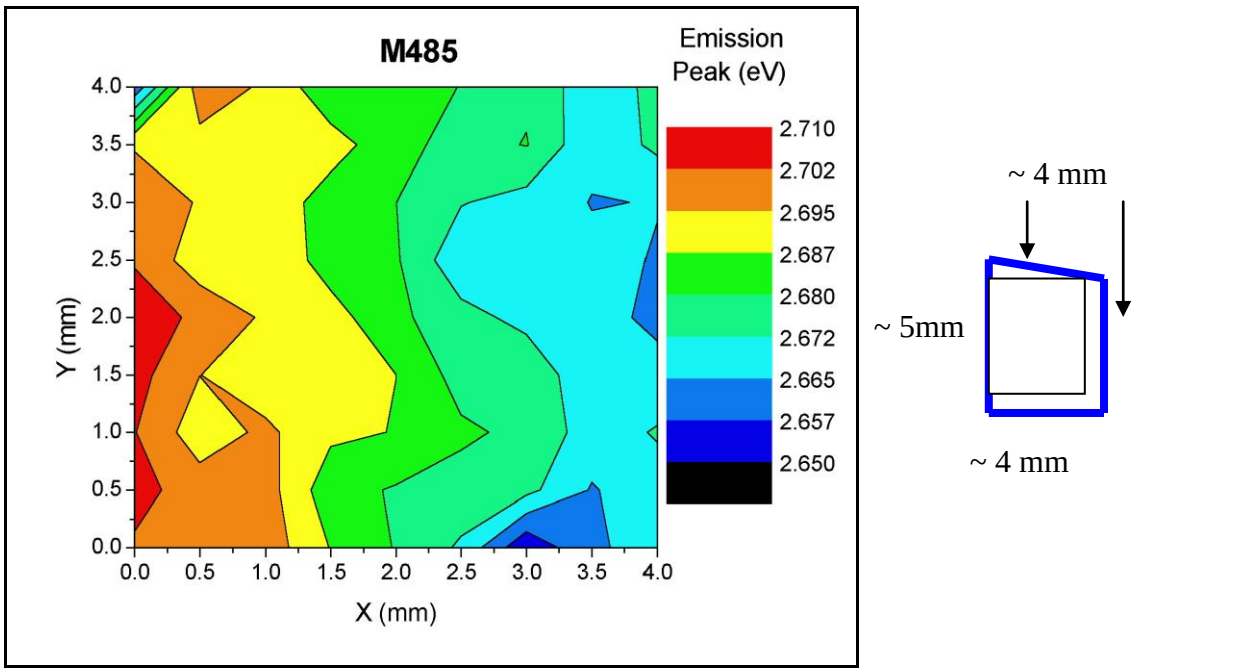

Figure 3.3 (d)

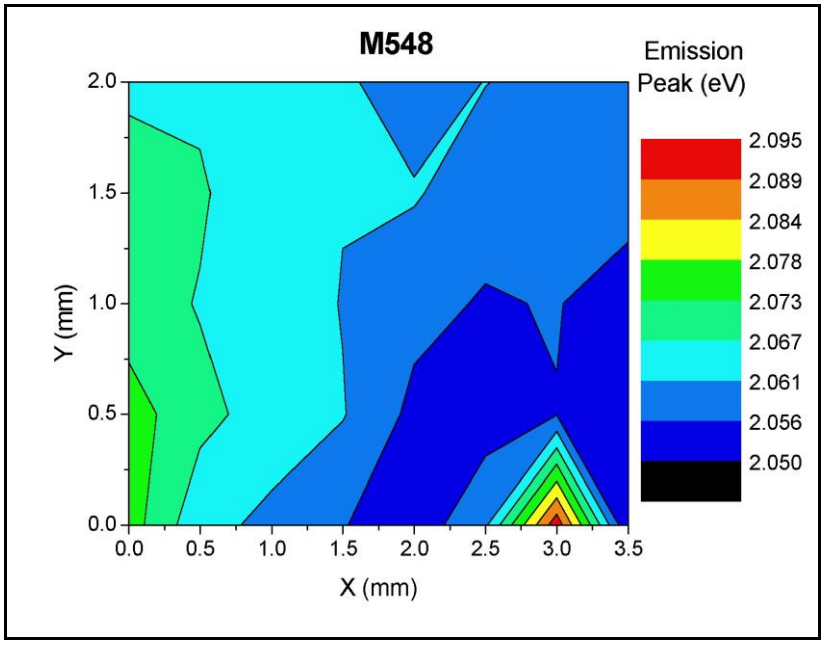

Figure 3.3 (e)

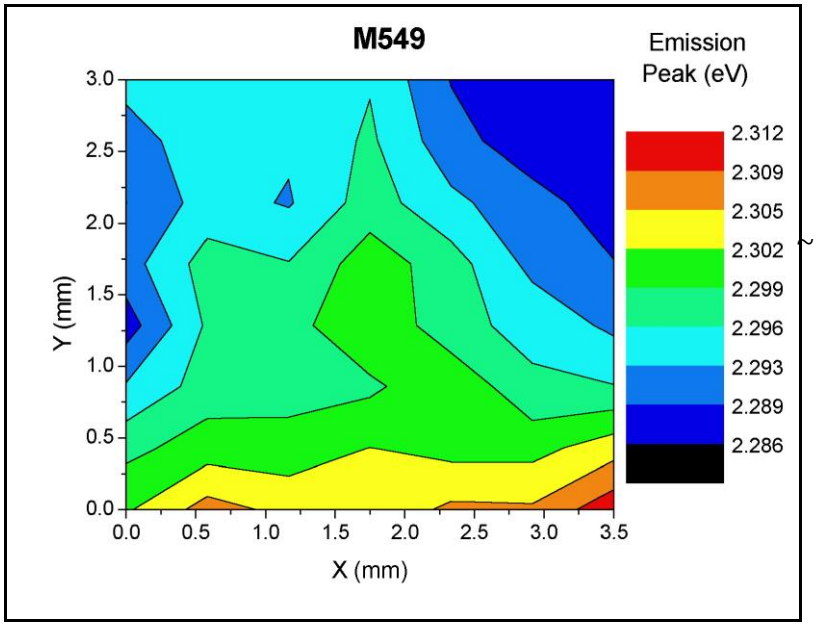

Figure 3.3 (f)

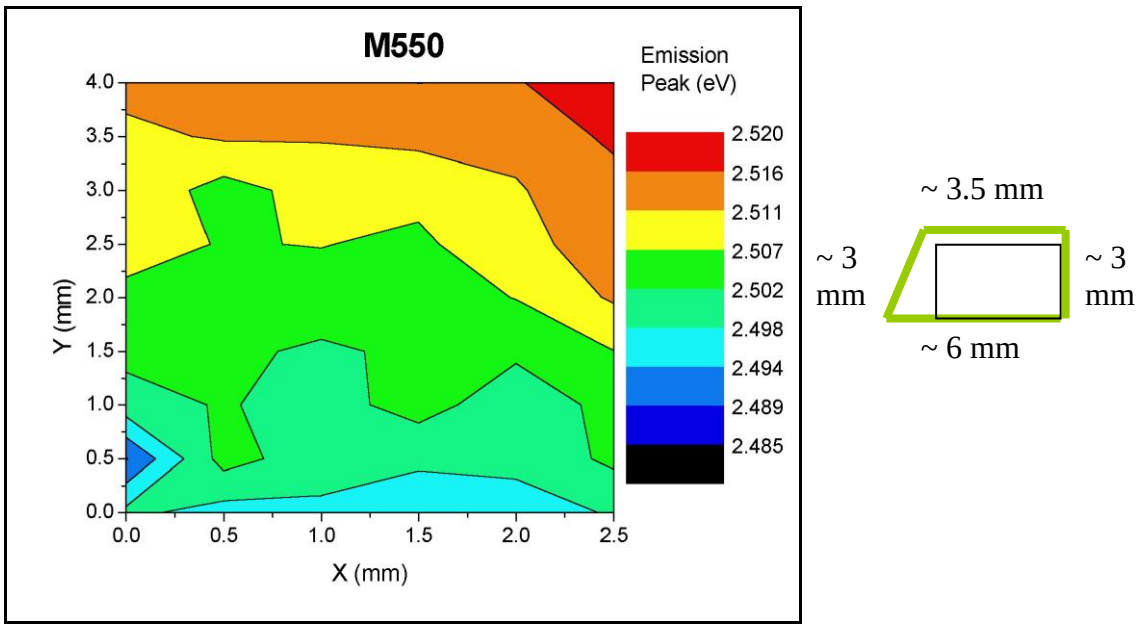

Figure 3.3 (g)

3.3 ASSESSING SAMPLE QUALITY

In order to assess the luminous efficiency of the samples, their emission intensities were first measured at low temperature (16K) and room temperature (300K) in the PL set up presented in chapter 2. The intensities, normalised to 100 for the sample with highest intensity, and the ratio I (16K)/I (300K) are shown in figures 3.4 and 3.5.

We found that all the samples emit light in the whole range from 16K to 300K. It is possible to see, in the graphs presented, that the samples belonging to the 5-series are more efficient than those of 4-series at low InN fraction. The intensity is bigger at low temperatures for 5-series and the ratio of intensity between the extreme temperatures (16K and 300K) is bigger in 4-series, which show a larger loss of intensity when the temperature is increased. These results are in accordance with

those presented in [18-20]: in general, the use of a MOVPE GaN template substantially increases the efficiency of the MBE InGaN epilayers.

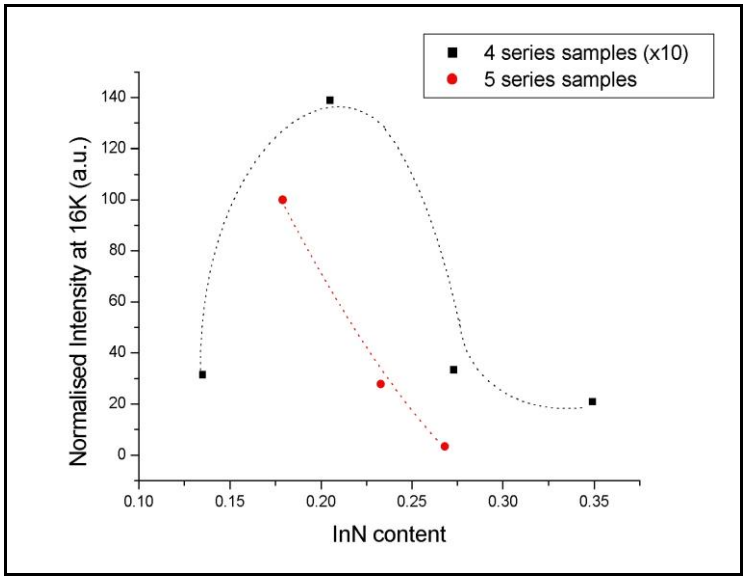

Figure 3.4. Normalised Intensity at 16K. Dotted lines are a guide to the eye

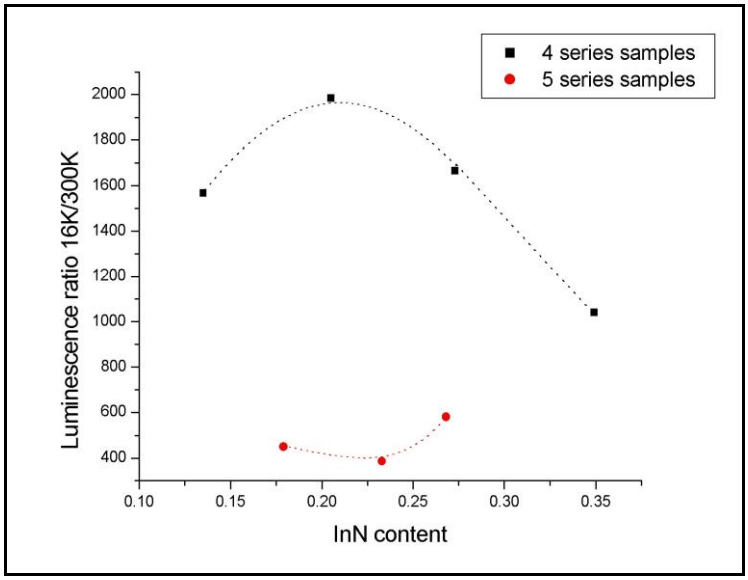

Figure 3.5. Ratio of luminous intensity I (16K)/ I (300K). Dotted lines are a guide to the eye.

We can also present, as a measure of the quality of the samples, the values for the broadening of the absorption edges as a function of the InN content of the

samples. These data were taken at room temperature in the absorption set up described in paragraph 2.1. The results are plotted in the graph shown as Figure 3.6.

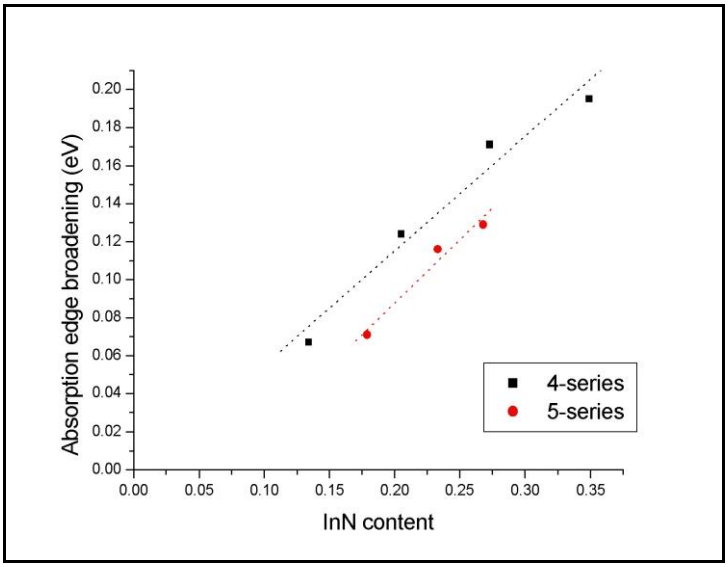

Figure 3.6. Broadening of the absorption edge

The broadening increases for both sets approximately linearly with the InN fraction. However the broadening is smaller for 5-series than for 4-series samples: for a given InN content, '4' samples are broader by ~50%. This shows the superior quality of samples grown on MOVPE GaN templates.

3.4 OPTICAL PROPERTIES AT LOW AND HIGH TEMPERATURES

PL, CL and optical absorption measurements were carried out in order to determine the optical energies of the samples, such as emission energy peak at various temperatures and bandgap energy at room temperature. PL measurements were taken both at 16K and 300K respectively while CL and absorption could only be performed at room temperature. Beam voltages of 6kV and 9kV were used in

order to obtain the CL data. With these voltages, 90% of electrons in the beam are absorbed at depths of, approximately, 150 nm and 300 nm respectively. The beam current was of the order of 10nA.

Figures 3.7 and 3.8 show CL and PL spectra, measured at 300K and 16K respectively. In Figure 3.9 we plot the variation of FWHM with InN content for CL. Figures 3.10 and 3.11 show how peak emission energies and bandgap energy depend, as well, on the InN fraction of the sample.

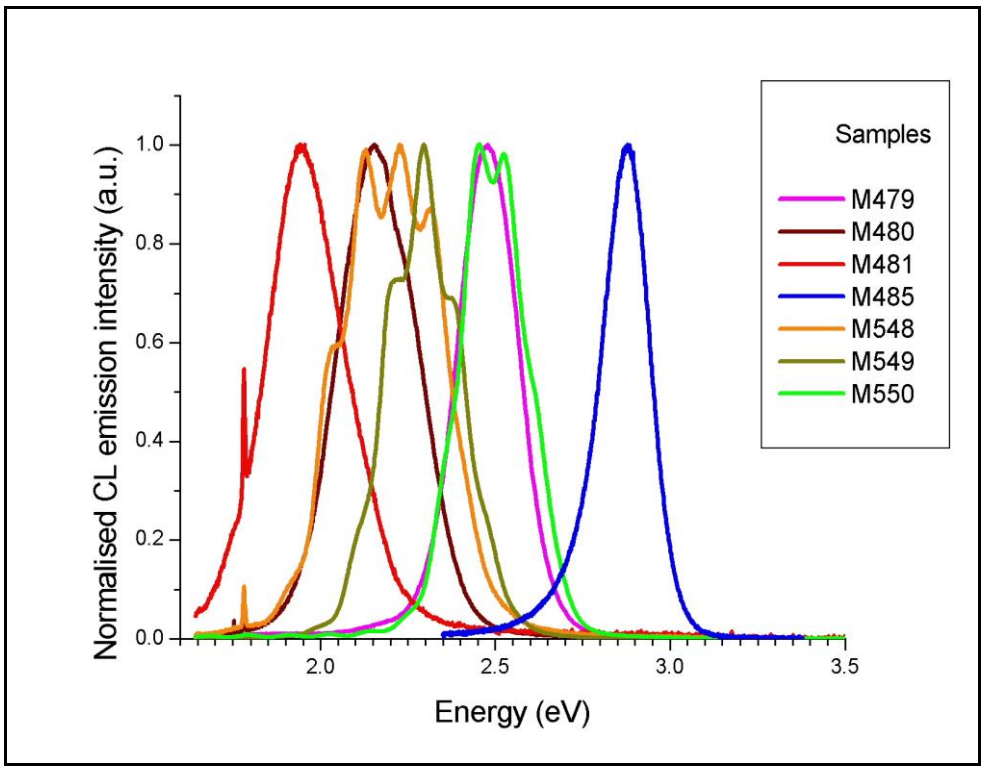

Figure 3.7. CL spectra taken at 300K with a beam energy of 9kV

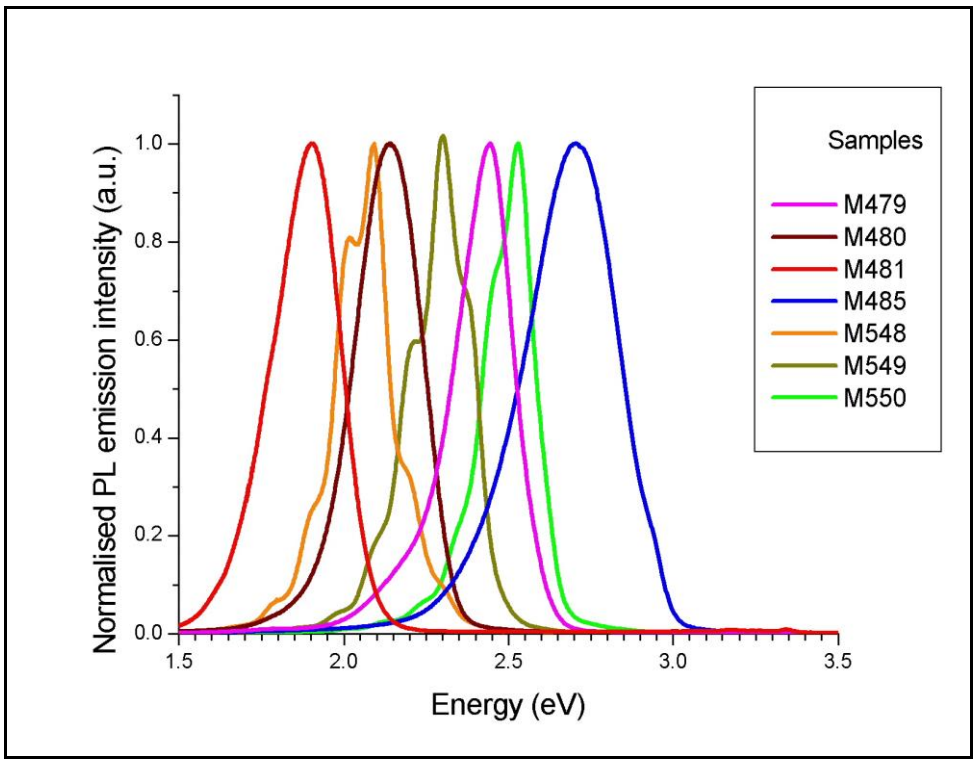

Figure 3.8. PL spectra taken at 16K

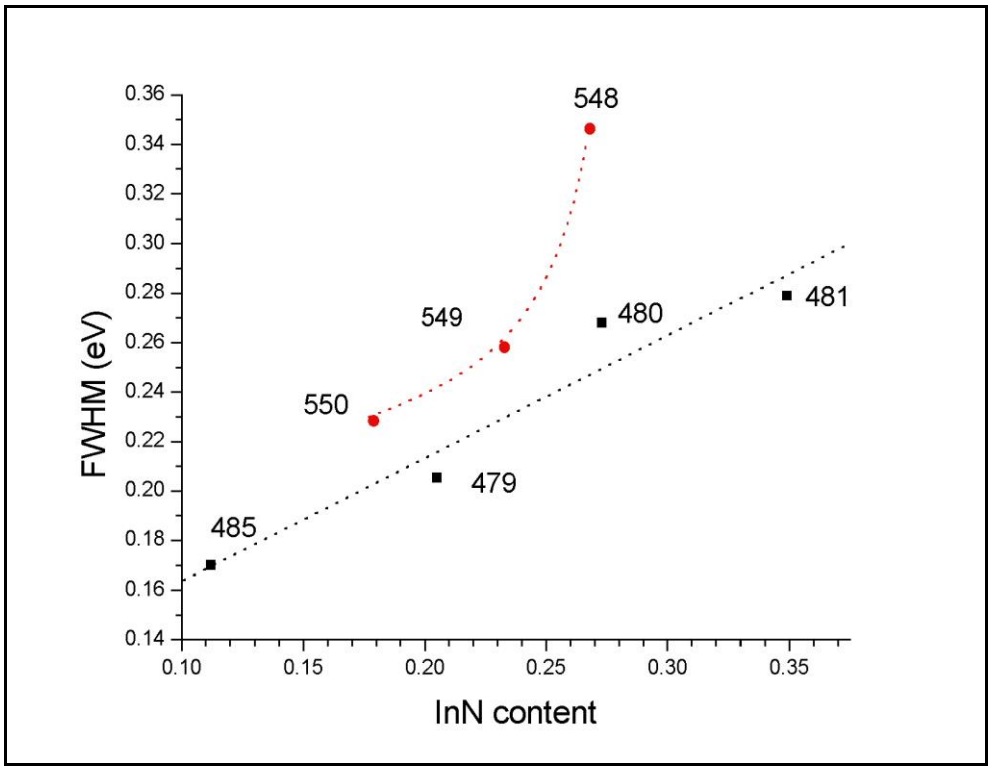

Figure 3.9. Room temperature CL's FWHM dependence on InN content

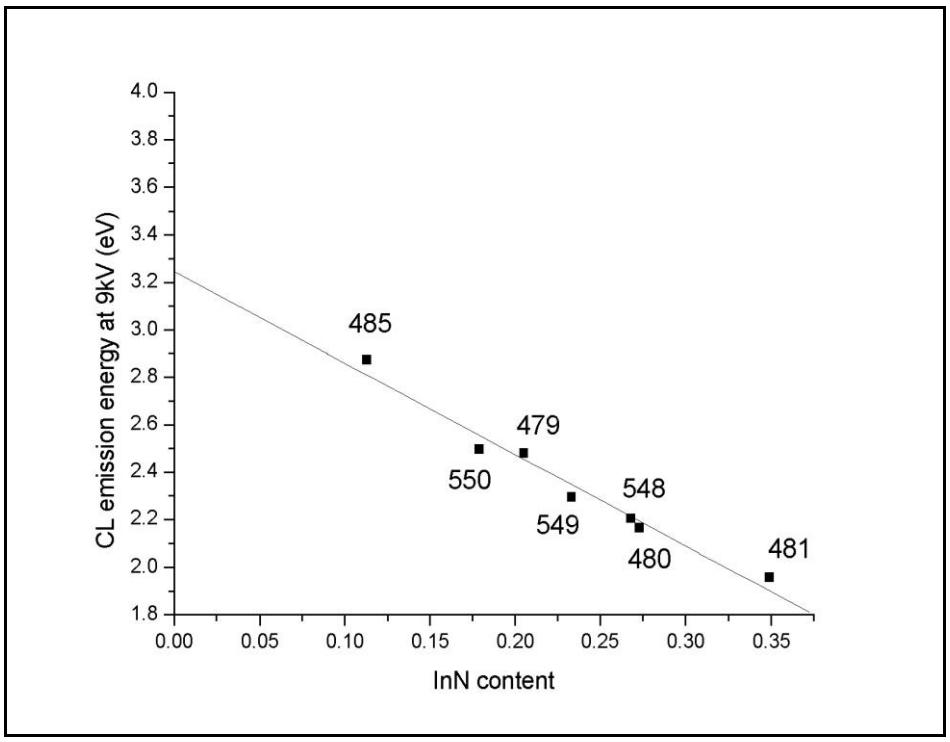

Figure 3.10. Dependence of CL emission energy on InN content at 300K

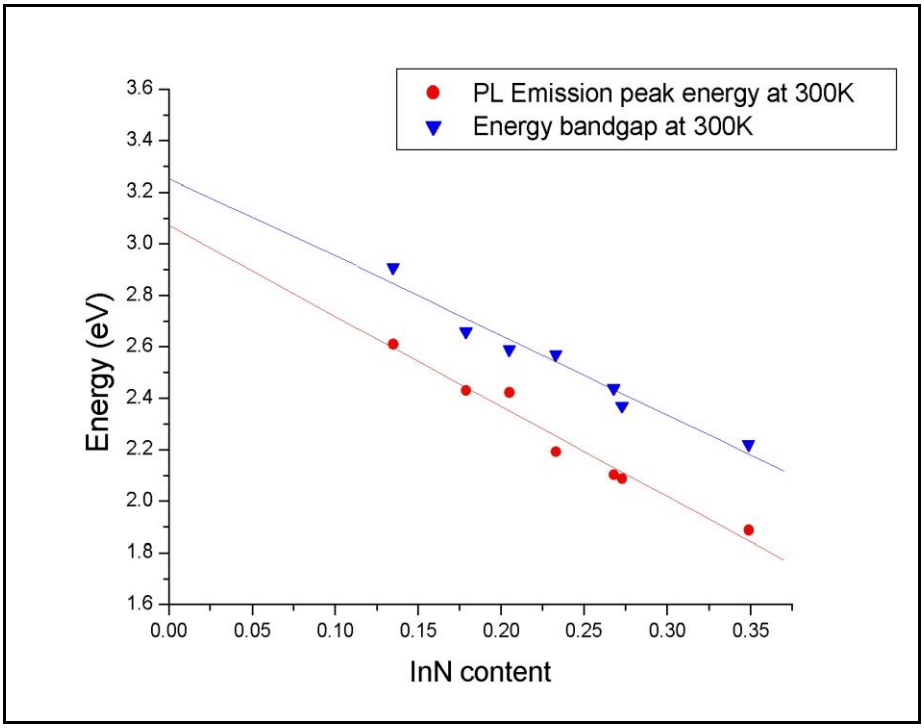

Figure 3.11. Dependence of PL emission energies at 16K and 300K and bandgap energies at 300K on InN content. Lines are best straight-line fits to the data sets.

The CL spectra shown in Figure 3.7 possess the same general shape: a single broadband feature with approximately exponential tails; in the case of samples belonging to the 5-series interference fringes are observed. The FWHM of the emission spectra broadens from 0.17eV in the case of the sample with the lowest InN content to 0.28eV for sample M481, the one with the largest amount of InN. Thus the FWHM of the CL spectrum increases with the amount of InN as it can be seen on Figure 3.9. The value obtained in the case of sample M548 is situated further away from the others. We could think about some interference with the GaN 'yellow band' since it emits in the same region.

A decrease of the peak emission energies with the InN content is observed in Figure 3.10 in the case of CL and in Figure 3.11 for PL, both at low and room temperature. In Figure 3.11 the bandgap energies at room temperature, obtained in the absorption measurements, are also plotted. A linear trendline could be fitted to the data. The value obtained for zero InN content is below the expected GaN wurtzite bandgap in all cases. At room temperature, the Stokes' shift decreases with InN fraction, but does not vanish as expected at $x = 0$.

3.5 TEMPERATURE DEPENDENCE OF PL EMISSION

A study of PL emission dependence on temperature was carried out in order to know how the temperature affects the luminescence properties of the materials studied.

The samples are introduced in the cryogenic chamber for performing the measurements of PL emission at different temperatures, which are selected by the

temperature controller. After waiting the time necessary for the stabilisation of the temperature in the cryogenic chamber, the measurements can be taken. Some of the results obtained are shown in Figures 3.12 (a)-(d); they have been plotted in a logarithmic scale in order to show more clearly how the change in temperature affects the luminescence properties of the samples.

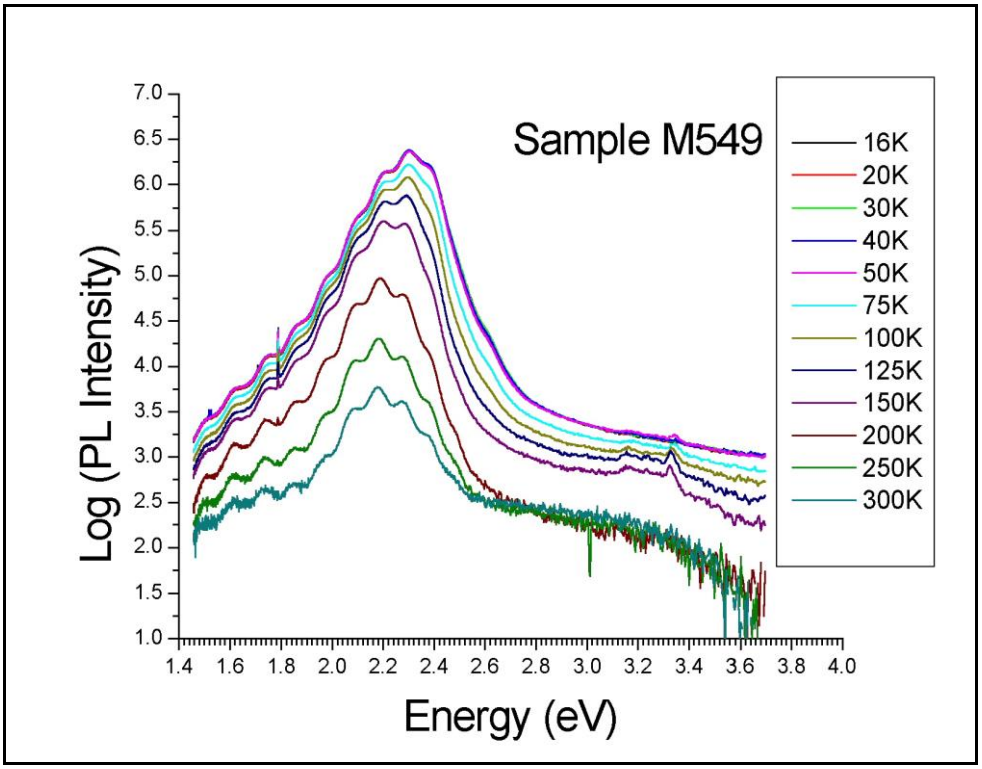

Figure 3.12 (a)

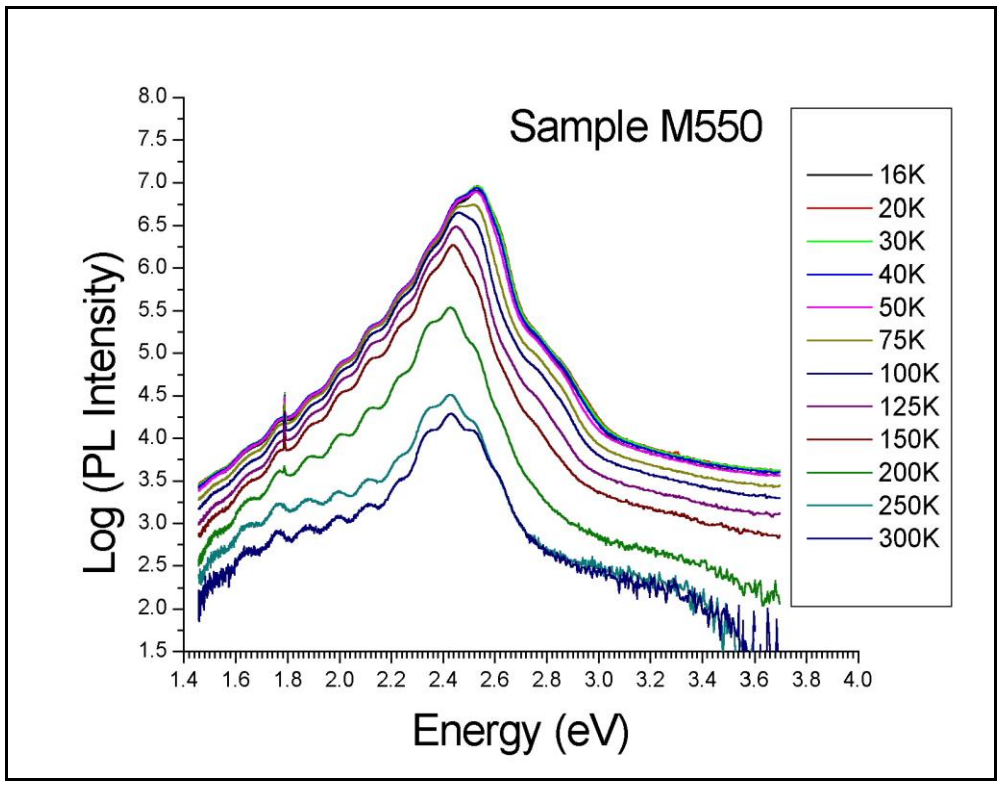

Figure 3.12 (b)

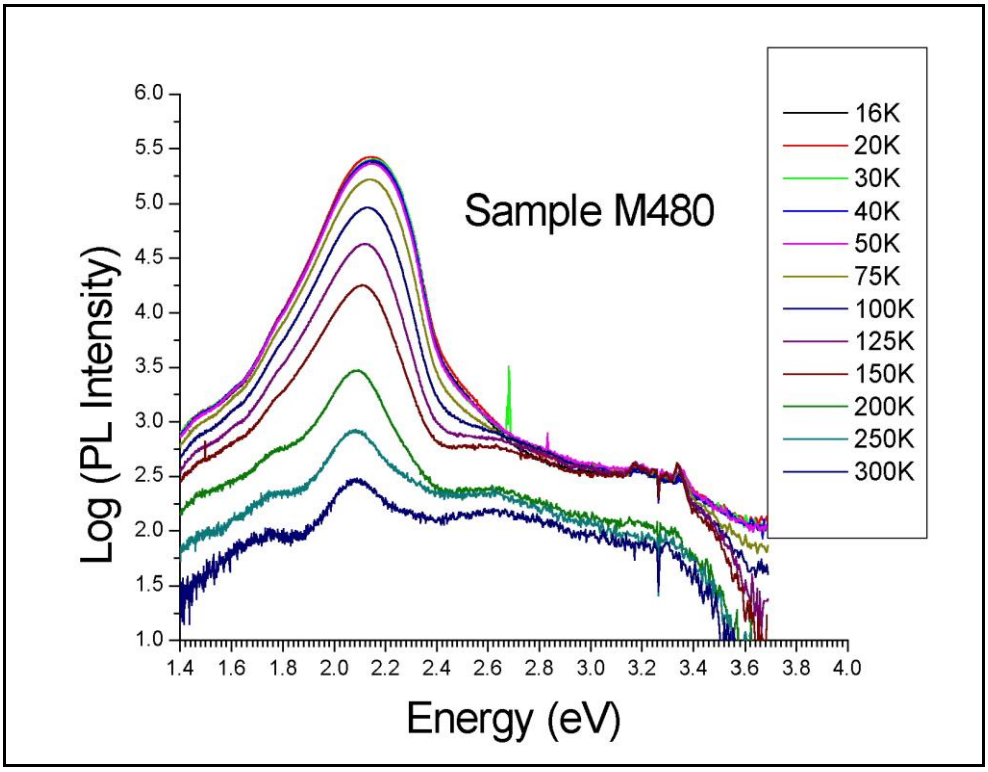

Figure 3.12 (c)

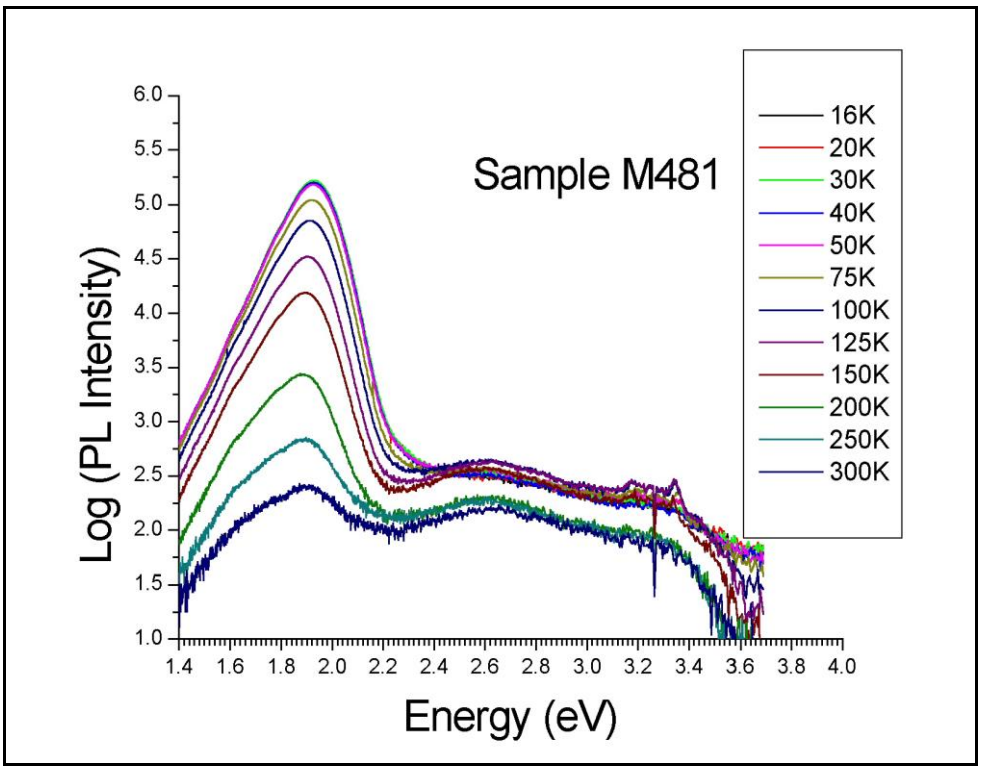

Figure 3.12 (d)

A high-energy emission peak with exponential tails dominates all the spectra and interference fringes are present up to energies of around 2.4-2.6eV. Periodic fringes with the same spacing have been also found in the absorption measurements. These results will be analysed in more detail in the following chapter.

3.5.1 Activation energy

It is observed in graphs presented in Figure 3.12 (a)-(d) that a decrease in intensity is a general feature expected in temperature dependence measurements. While increasing the temperature the number of carriers decaying radiatively decrease; this behaviour can be explained taking into account the three energy level

model presented in chapter 1 (see Figure 1.9). The experimental data have been fitted using the equation (1.9). The results are shown in Figure 3.13

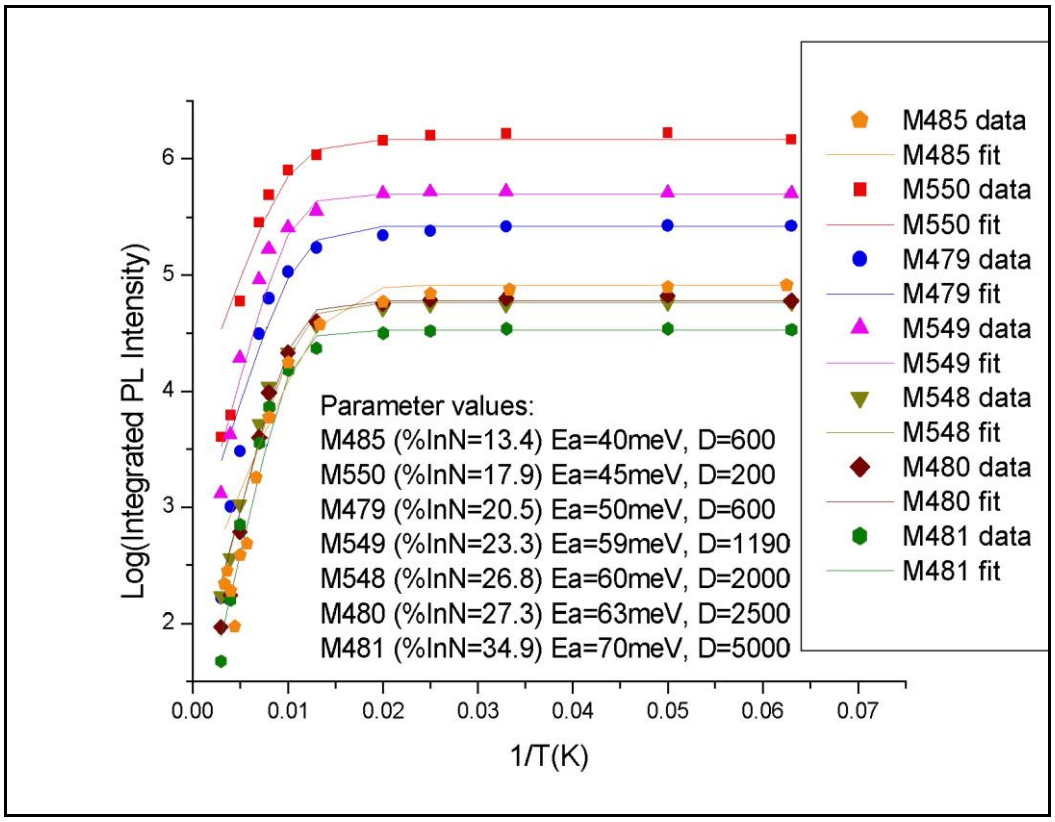

Figure 3.13. Fit to the temperature dependence data

The fits are better for those samples with higher InN content because the drop of the points when increasing the temperature is not as abrupt as in samples with low InN content.

3.5.2 Peak emission energy and width dependence on temperature

While increasing temperature another features were found in common to all the samples, such as a shift in the emission energy, a change in the width and a decrease in the integrated intensity.

Both peak emission and full width at half maximum (FWHM) are plotted as a function of temperature. The curves have been fitted using equation (3.1), presented in paragraph 3.2. Some of the results obtained are shown in Figures 3.14 (a)-(d).

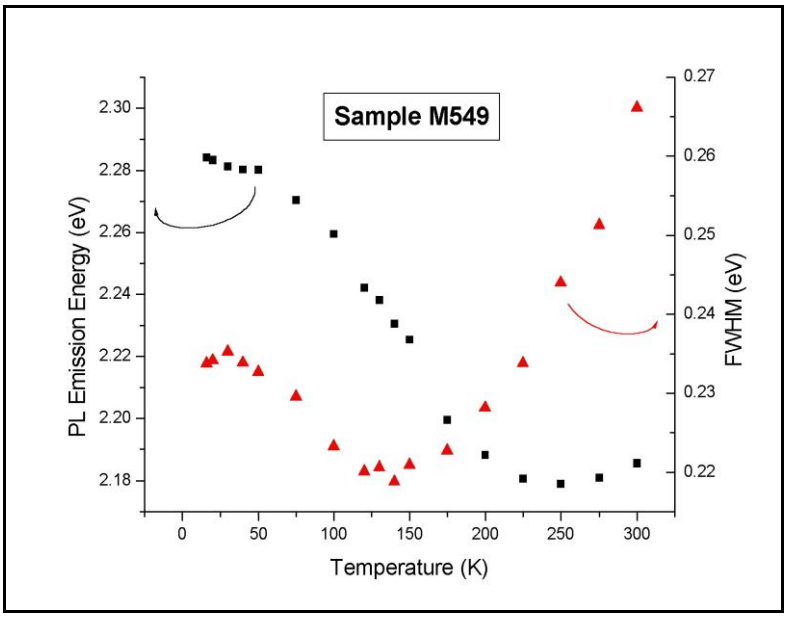

Figure 3.14 (a)

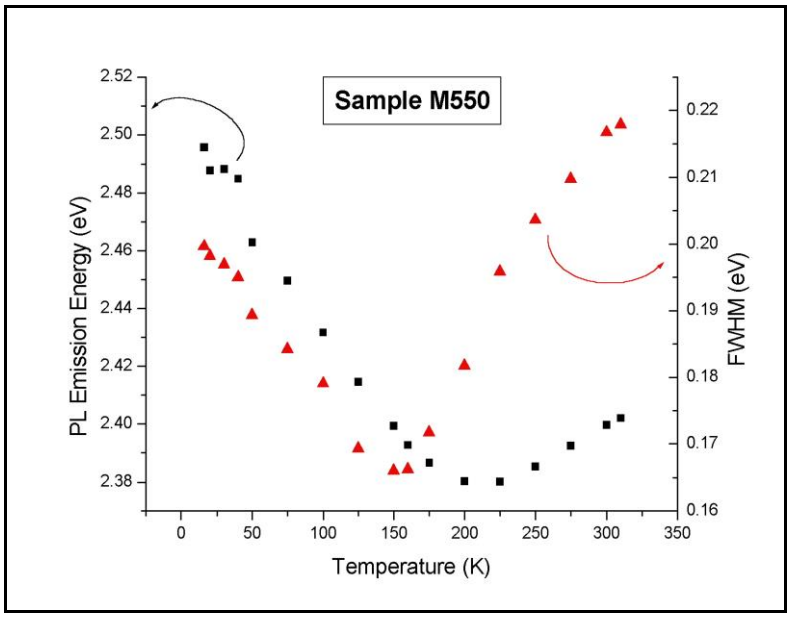

Figure 3.14 (b)

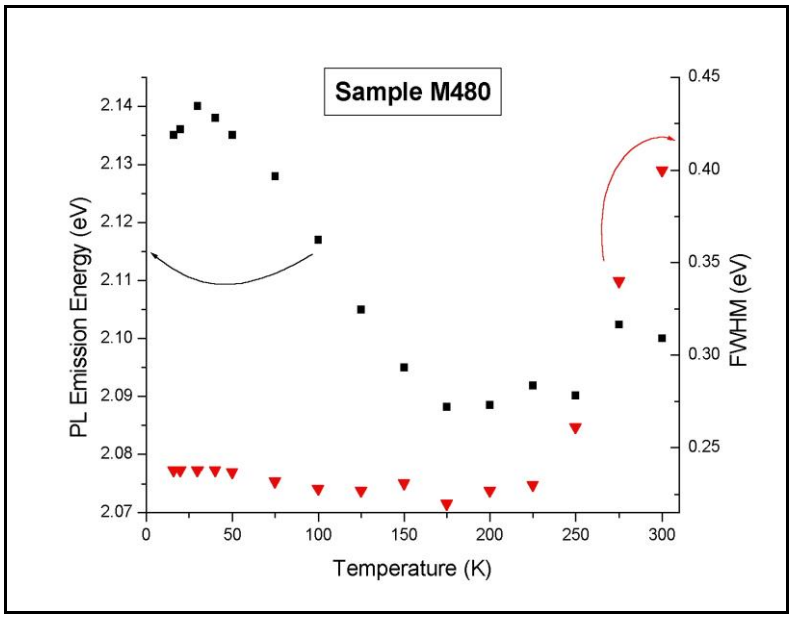

Figure 3.14 (c)

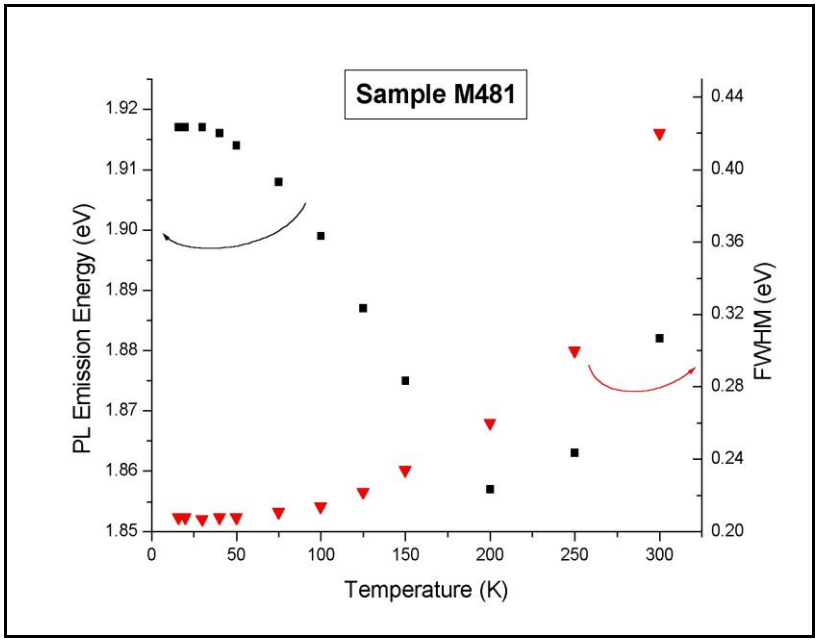

Figure 3.14 (d)

In both series the same shift in emission energy can be observed: first a red shift is detected followed by a blue shift at bigger temperatures. Minima in FWHM

have also been found with the increase of temperature. These results are in agreement with those ones reported by F.B. Naranjo et al [14,21].

We can also observe that the emission energy shifts from low temperature to room temperature are bigger in samples belonging to the 5-series (around 0.1eV) than for those in 4-series (around 0.06eV at most) except for sample M485. In this one the shift between photoluminescence emission energy at low temperature and room temperature is as big as in 5-series: around 0.1eV.

4. DISCUSSION

The aim of this chapter is to analyse the results presented in the third chapter. Some important features such as the quality of the samples, their emission properties and their dependence on the InN content and temperature will be discussed.

4.1 HOMOGENEITY AND QUALITY OF THE SAMPLES

Luminescence was obtained in all samples, even at room temperature. This is a general indicator of good sample quality. However, as pointed out in Chapter 3.1, the efficiency of samples in the 5-series is generally larger than in the 4-series: as well as brighter luminescence at low temperatures, 5-series samples show less quenching when the temperature increases. As can be seen from Figure 3.4, the luminescence intensity decreases with the InN fraction, apart from sample M485. The same tendency can be deduced in the case of 4-series for the ratio between luminescence at low and room temperature, I(16K)/ I(300K), presented in Figure 3.5: the quenching of luminescence increases with InN content. The 5-series does not present a special tendency in this respect.

Another quality factor is the width of the peak and the broadening of the absorption edge. As was shown in Figure 3.6 the broadening of the absorption edge is smaller for samples belonging to the 5-series; the bandtail states are less numerous in 5-series samples. Regarding the width of the emission peak, this factor is related to the localisation of the exciton and its lifetime. A general tendency can not be plotted but FWHM generally increases with the amount of InN in the samples.

Comparing the CL and PL data there is one sample whose spectral properties are anomalous: M485. Not only is the width changed but also the emission peak energy, as can be seen by comparing Figures 3.7 and 3.8. A possible reason for this difference in width and peak energy is the inhomogeneity of InN content with depth revealed in Figure 3.1. The InN content of M485 decreases with depth. In consequence the peak energy shifts to smaller energies in PL, which addresses the whole sample thickness. We should expect the same behaviour appearing in the other sample that presents a variation of InN with depth, M481. But no change in the position of the peak or in the width is observed in this case.

We also have to take into account that these comparisons between CL and PL results are made at different temperatures: 16K in the case of PL and 300K for CL. A comparison between the widths obtained at room temperature by PL and CL has been done. The result is shown in Figure 4.1. While the linewidths for samples belonging to the 5-series are almost the same, in the case of 4-series samples they increase for PL. This result is another quality factor for 5-series samples and another factor against sample M485 whose width increases drastically from CL to PL. Since PL mappings on individual samples showed no large lateral inhomogeneities, it is not possible to attribute the increase of linewidth of PL over CL at room temperatures of 4-samples to such inhomogeneities.

We could partly explain the differences between CL and PL measurements if we take into account the different excitation power per unit of area applied in each case. The electron beam used to perform the CL measurements has a diameter of the order of 100nm; for a voltage of 1kV and an intensity of 10nA the power incident on the samples is of order $10kW/cm^2$. On the other hand, the diameter of the spot for the

laser used in the PL set up is of order 10μm. With a laser of power 1mW, the incident power density is of the order of 100W/cm^2. Two orders of magnitude separate the power density used in PL and CL measurements.

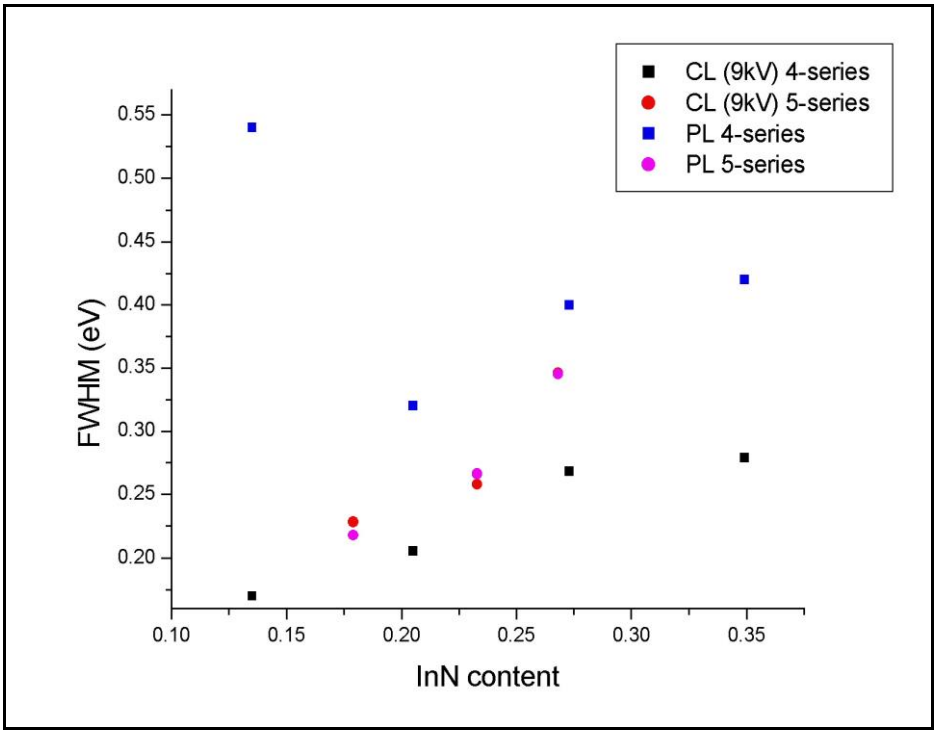

Figure 4.1. PL and CL FWHM at 300K

High powers lead to high carrier densities. When samples are efficient enough, as 5-series samples, the linewidth of the peak obtained does not depend too much on the power. It does if the efficiency is low: a lack of power excitation decreases the filling of levels for efficient radiative decays and the line broadens.

In summary, a comparison between the quality of the samples has been performed, showing that the 5-series has, in general, a better performance than the 4-series, while an increase of InN content generally decreases luminescence quality in the range $0.13 < x < 0.35$. The brightest sample is found to be M550, with 17.9% InN

fraction. M485, in spite of its lower InN content, which should have made it a better sample according to the literature, turned out to be the one with the worst performance due to a vertical inhomogeneity of InN fraction.

4.2 INFLUENCE OF TEMPERATURE ON THE EMISSION OF MBE-GROWN InGaN

Both sets of InGaN samples show Fabry-Perot fringes, caused by interference between reflections or emissions that originate at the surface and interfaces of the samples. Depending on the series, different layers are found to be responsible: it is possible to deduce this because the fringe spacing depends on the series.

In order to calculate the thickness of the layer causing the interference fringes we use the following equation [38]:

$$t = \frac{1}{2nd} \tag{4.3}$$

where d is the spacing between fringes observed in the spectra (energy units), n is the refractive index of the material and t is the thickness of the layer (length units), which is causing the interference patterns.

The refractive index for GaN is calculated using the following equation [39]:

$$n(h\upsilon) = \left(\frac{h\nu}{E_g}\right)^{-1}\left\{a\left[2-\left(1+\frac{h\nu}{E_g}\right)^{\frac{1}{2}}-\left(1-\frac{h\nu}{E_g}\right)^{\frac{1}{2}}\right]+b\right\}^{\frac{1}{2}} \tag{4.4}$$

where h is Planck's constant, ν the light frequency, E_g the direct energy bandgap and a, b fit parameters, obtained from measured refractive index spectra of the compounds. The GaN values of a =9.31 and b = 3.03 were used in all calculations.

For the 5-series the value of fringe spacing is around 100meV, in every sample. That gives us, with a value for the refractive index of InGaN close to 2.3, a thickness for the layer causing the interference of 2.7μm.

In 4-series the fringe spacing is bigger. In the PL system they can be difficult to see. It is easier to calculate the thickness from the absorption data. In this case the distance varies between 300meV (measured in the spectra of samples M479 and M480) and 400 meV (for samples M481 and M485). That means that the layer causing the interference should have a thickness of around 0.89μm in the first case and 0.67μm in the second case.

According to the scheme shown in Figure 1.7, the fringes could be caused in 5-series samples by interference between the surface and the bottom substrate/nitride interface: layers of MBE InGaN layer (0.3μm), MBE GaN buffer layer (0.4 μm) and MOVPE GaN template (2μm) together give a total thickness of 2.7μm. In 4-series it would be only the MBE InGaN layer (0.3μm) and the MBE GaN buffer layer (0.4μm) which, acting together, would cause the interference.

In the case of the PL, these fringes appear only up to energies of 2.4eV to 2.6eV. For energies bigger than these values the curves of all spectra are smooth, and a "blue" background appears centred on 2.7eV, approximately. This band appears both in 4 and 5 series being M548, M480 and M481 the samples in which it is easiest to see. The disappearance of the fringes may be due to the absorption of blue light by

the active InGaN layer, taking into account the fact the energies at which the fringes disappear are close to the absorption edges of InGaN samples.

4.2.1 Activation Energy

It was shown in paragraph 3.4.1 that the number of radiative recombinations decreases when the temperature increases. The fitting of experimental data to equation (1.9) shows the activation energy increases with InN content. This indicates deeper localisation of carriers if we assume that the non-radiative level represents *delocalised* states. The data can be fitted to a disorder/localisation model as is shown in Figure 4.2.

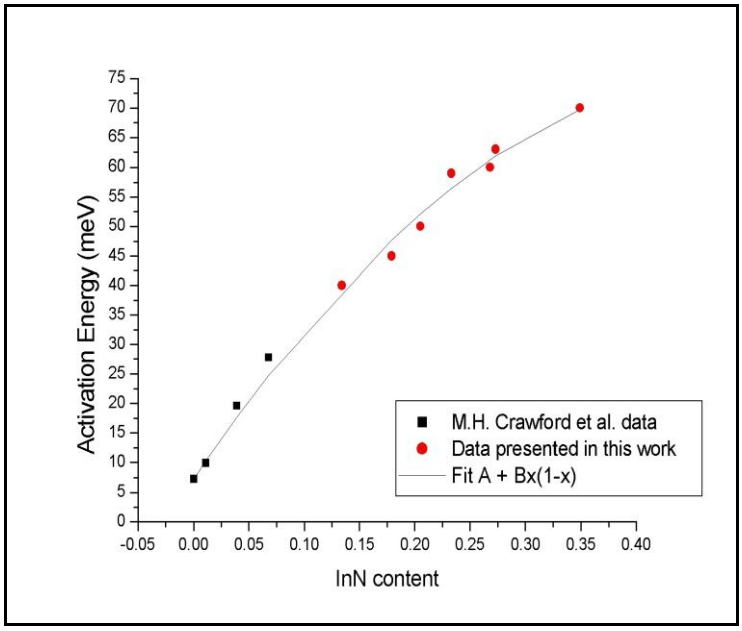

Figure 4.2. Fit of the activation energy dependent on InN fraction

In this model the activation energy would be proportional to the product of InN and GaN fractions on the sample. It would increase until x=0.5 and show a further decrease for $0.5 < x < 1$. With the data available we only can validate this model up to x = 0.35. Earlier measurements of activation energy by Crawford and co-workers [40] showed an approximately linear trend. The figure shows that Crawford's results are also compatible with our model since $x(1-x) \sim x$ at low values of x.

4.2.2. Peak emission energy and width dependence on temperature

In Figures 3.14 (a)-(d) the variation of both the emission peak energy and the FWHM of four samples are plotted.

All of the samples present an anomalous behaviour with temperature: an emission redshift followed by a blueshift appear when increasing the temperature, results that are in agreement with the literature [14,21]; the minima found in the FWHM are, generally, deeper in 5-series samples.

The phenomenon of red-blue-red shift in the peak emission with temperature, accompanied by a decrease and an increase in the linewidth, is known as "S-shape behaviour" and has been explained in terms of localisation of carriers and their lifetimes by Cho et al [41].

We could explain this behaviour by extending the three level model presented in Figure 1.9, to let B represent a band of different allowed states which are identified with the different minima existing in the conduction band. In the model we have to make some assumptions about the lifetime of the carriers in order to explain

completely this behaviour. We will have ground in previous work [41]. In the time-resolved measurements taken in [41] it is shown that the lifetime increases during the emission redshift, reaching a maximum at the same temperature as the minimum in emission energy and decreases quickly during the following emission blueshift.

Assuming this lifetime behaviour and a constant filling of carriers we can say that at low temperatures the carriers are frozen in the different degenerate levels in B. In consequence the radiative decays are produced from different states. The PL emission peak is a weighted average of these decays. When temperature increases the thermal energy of the carriers allows them to interchange among radiative levels while the energy difference between A and B decreases with the bandgap [42]. The carriers thermalise among these levels and, taking into account the lifetime reaches its maximum value, they have time for recombining radiatively from the most favourable states, those closest to the ground level A; that would explain the redshift and the minimum in the FWHM. A further increase of the temperature would give the carriers enough thermal energy to travel to the non-radiative band (C); the thermal energy would also affect the internal decays in the radiative levels. Due to the temperature and the fast decrease of the lifetime, the carriers would not have time to travel to the most favourable state; in consequence the decays would not be produced from the same level in B. Thus, the peak emission energy increases and FWHM broadens.

Both minima, FWHM and emission energy, usually occur at different temperatures for our samples. That could be due to different localisation centres. The temperatures at which the minima appear and also their "energy depth" (ΔE), that is, the energy difference for the emission between 16K and the temperature at which the

minimum is reached, are shown in Table 4.1. Although a dependence of the appearance of these minima with InN fraction has not been found, we could say, regarding 5-series samples, that ΔE increases when the InN fraction decreases. The values are always bigger than kT at room temperature (~25meV).

Perhaps it would be necessary to think about the growth conditions of the samples as an important factor in order to find an explanation for the different temperatures at which the minima in emission peak energy and FWHM appear.

Sample	InN content	Emission energy minimum (K)	FWHM minimum (K)	ΔE (meV)	ΔFWHM (meV)	Ea (meV)
M548	0.268	~ 150	------	~ 35	------	60
M549	0.233	~ 250	~ 140	~ 105	~ 15	59
M550	0.179	~ 210	~ 150	~ 115	~34	45
M479	0.205	------	------	------	------	50
M480	0.273	~ 175	~ 175	~ 52	~ 18	63
M481	0.349	~ 200	------	~ 60	------	70
M485	0.135	~ 200	~ 70	~ 260	~ 16	40

Table 4.1

4.3 INFLUENCE OF InN CONTENT ON THE EMISSION PROPERTIES

As pointed out in the previous chapter, a measurement of the InN content of the samples was performed in the EPMA with different beam voltages, which explore different depths. At a fixed depth (Z), the InN fraction is found to be fairly

constant in the other two dimensions (X and Y) for all samples. For most of the samples this content is invariable with depth but samples M481 and M485 are exceptional.

The increase of InN content in the epilayers has two general consequences: an increase of the linewidth and a shift of the emission peak energies to lower values. Regarding the broadening of the linewidth, it would be generated by two factors: fluctuation in composition and (random) electric fields created by piezoelectric effect in the alloy [43]. The first factor would have a weak contribution according to theoretical calculations [44]. The piezolelectric field, high enough due to the polar nature of III-N, together with localisation would be the main determinant of the broadening. The electric field tends to separate the carriers and they get trapped in the different local minima, when they recombine. FWHM broadens because the recombinations take place at different minima.

On the other hand the fits of the activation energy presented in Figure 3.13 show a deeper localisation of carriers with larger InN content: i.e. the activation energy increases with InN fraction.

4.3.1 Comparison between MOCVD and MBE epilayers

In Figures 4.2 and 4.3 the PL and CL emission energies of MOCVD- and MBE-grown samples are compared, where MOCVD results are taken from previous research done in the Semiconductor Spectroscopy and Devices group at the University of Strathclyde [27,45]

Systematic differences between MOCVD and MBE samples are observed, both for PL at low temperature and CL at room temperature. The relevant data are presented in Figures 4.3 and 4.4. In both cases the best lines fitting MOCVD and MBE data have a very similar slope but different intercepts for zero InN content as shown in the table of Table 4.2. Thus, epilayers in the same range of InN content present quite different emission peak energies. MBE data are shifted to smaller emission energies compared to MOCVD layers with the same InN content.

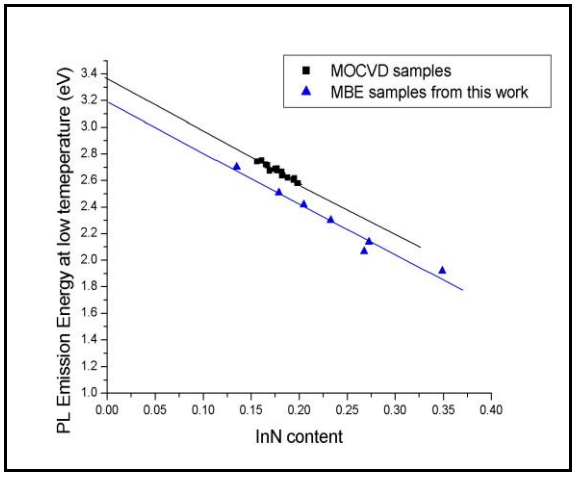

Figure 4.3. PL Emission Peak Energies at low temperature of MOCVD- [45] and MBE-grown InGaN epilayers

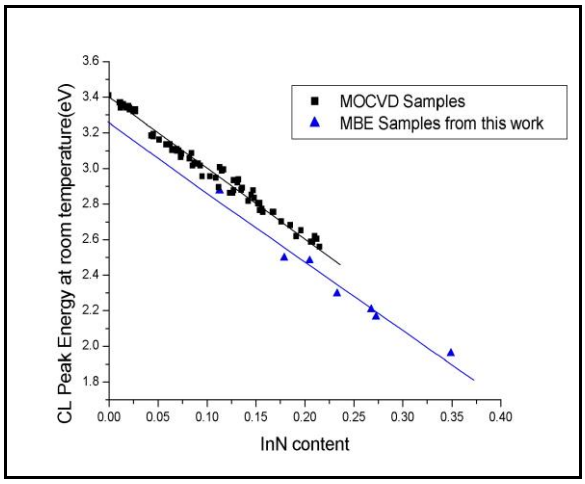

Figure 4.4. CL Emission Peak Energies at room temperature of MOCVD- [27] and MBE-grown InGaN epilayers

	PL (<25K)	CL (300K)	Absorption bandgap (300K)
MOCVD	3.37 (5)	3.40 (1)	
MBE	3.18 (8)	3.24 (7)	3.26 (7)

Table 4.2. Intercepts of best-fit lines for x=0. Energies shown are in eV and the numbers in parentheses are the errors related to the linear fits

As it was pointed out in paragraph 1.2.2 the bandgap energy is not expected to vary linearly with InN fraction. It should obey equation (1.5) in the case of an alloy. Two different fits of this equation to the room temperature data presented in Figure 3.12 were compared. The expected value for the InN bandgap was fixed at 1.9eV and 0.67eV, respectively, and the GaN bandgap and the bowing b were considered to be free parameters. The results of data fitting to Eqn 1.5 are plotted in Figure 4.5. The bandgap value (at room temperature) for hexagonal GaN is reached when 1.9eV is chosen as the InN bandgap. The bowing parameter in this case is 3.06 ±0.33eV which, within the error margin, is in agreement with literature [30,31].

For 0.67eV the value reached for x = 0 is 3.32eV, closer to our experimental results for a linear fit, presented in Table 4.2, and to the value of bandgap for cubic GaN [46]. The bowing parameter in this case is 0.93eV. Since all of the fits are nearly overlapping in our data range it would be risky to select any fit as the best one. It would be necessary to have more data points related to InN fractions bigger than x=0.4, in the region where the different fits split up.

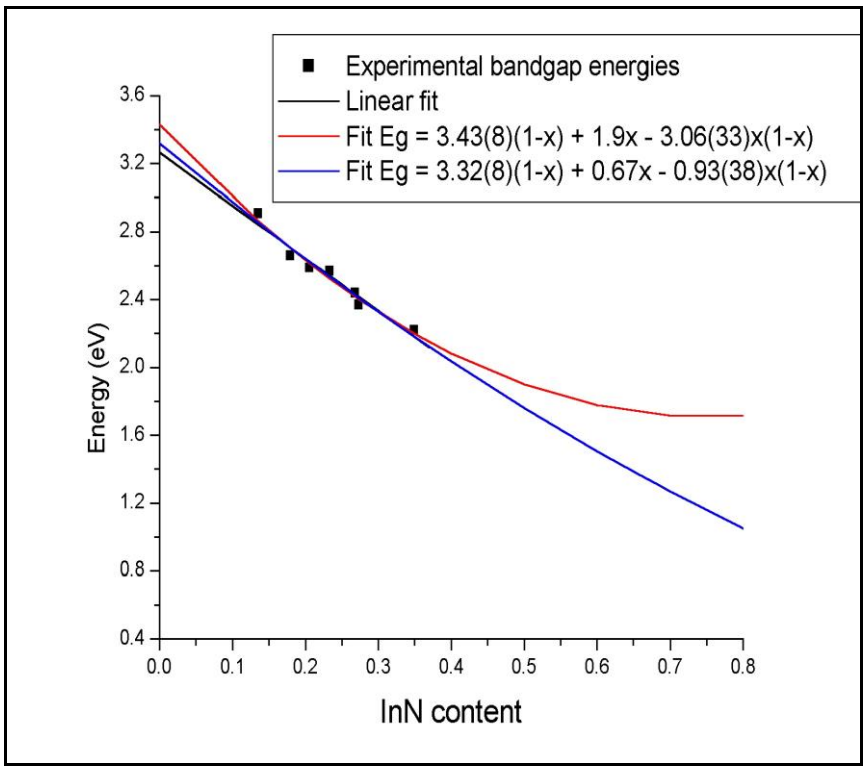

Figure 4.5 Bandgap energy fit assuming an InN bandgap values of 1.9eV and 0.67eV.

5. CONCLUSIONS AND SUGGESTIONS FOR FUTURE WORK

5.1 CONCLUSIONS

The study of emission properties of MBE-grown InGaN epilayers was the main aim of this report. Optical absorption, photoluminescence (PL) and cathodoluminescence (CL) spectroscopies were carried out in order to determine the optical energies of a range of samples: emission peak energy, in the case of PL and CL, and bandgap energy for optical absorption spectroscopy. Both absorption and CL data were taken only at room temperature (300K) while PL measurements could be performed at different temperatures from 16K to 300K.

It was found that samples grown over a MOVPE GaN template (the 5-series) are of higher quality: they are more luminous at low temperature by a factor of 10, they present a lower loss of luminescence when the temperature is increased and the broadening of the absorption edge is consistently smaller than in 4-series samples by ~50% for a given InN content. The emission linewidth is also constant for CL and PL measurements, contrary to 4-series samples whose linewidth increases in the case of PL. Although all the samples presented luminescence even at room temperature, M550 was the sample with the best performance. On the other hand sample M485, which was expected to be one of the brightest samples due to its low InN content (~13%), presented poor luminescence properties, its intensity being comparable to samples with an InN content of ~27%. This lack of luminescence could be caused by a poor growth; in fact, the InN content measured in M485 by WDX was found to vary with depth.

Regarding emission energies: a comparison with MOCVD samples in the range $0<x<0.4$ was accomplished. Two different tendencies could be discriminated both for PL and CL data. The best lines fitting MOCVD and MBE samples have comparable slope but different intercepts for zero InN content. In consequence we have a shift in the emission peak energy between MOCVD- and MBE-grown epilayers with similar InN fractions. In the case of MBE-grown InGaN epilayers the intercept x=0 is closer to the value of cubic GaN [46] but the presence of hexagonal GaN in the samples is irrefutable since we obtain a clear peak ~ 3.4eV in the room temperature absorption measurements.

On the other hand, as InN fraction increases redshift and broadening of both emission and absorption linewidths are observed. They could be explained by two mechanisms: localisation on spontaneously grown InN-rich QDs [47-49] and piezoelectric effects caused by the large lattice and thermal expansion coefficient mismatches between substrate and active layers [43].

Thus, both effects, localisation and polarisation, would affect the emission of InGaN devices and would be reflected on optical properties such as the shift on emission energy, the broadening of the emission linewidth and the broadening of the absorption edge.

A study of the dependence of luminescence with temperature has also been performed, studying the behaviour of integrated intensity, emission peak energy and emission FWHM. On one hand, regarding the dependence of the integrated intensity with temperature, we found that the activation energies, calculated by fitting data to Eqn. (1.9), increase with the InN fraction fitting according to the predictions of a disorder/localisation model for alloys. On the other hand, we also detected ”S-shape

behaviour" of the PL emission peak energy accompanied by the appearance, in some samples, of a minimum in the FWHM at lower temperatures than the emission minimum. They may be explained in terms of different localisation centres. A dependence of these minima on InN content has not been found. This behaviour can be partially explained by the three level model presented in the introduction chapter but still some experiments have to be carried out in order to complete the explanation.

5.2 FUTURE WORK

As written in paragraph 5.1, some experiments should be carried out in order to clarify the "S-shape behaviour". Time-resolved measurements would be necessary in order to know how the lifetime of the carriers depends on temperature. Measurements of the dependence with temperature of the bandgap and also experiments to determine the filling of radiative levels would help to explain the redshift-blueshift of the emission energy and FWHM with temperature.

On the other hand the data range of the results presented in this report could be extended to higher InN contents. Having more data better fits to the different optical energies such as activation, bandgap, PL and CL emission energies could be done. It would be ideal to work with InGaN samples grown on MOVPE GaN templates due to the better luminous quality they present.

REFERENCES

[1] D.A. Neamen, *Semiconductor Physics and Devices*, Irvin, United States of America (1992)

[2] J.S. Blakemore, *Solid State Physics*, Cambridge University Press, United Kingdom (1983)

[3] B. Gil, *Low-dimensional nitride semiconductors*, Oxford University Press, Oxford (2002)

[4] www.sei.co.jp/sn/2002/07/feature_article.html

[5] S. Nakamura and G. Fasol, *The Blue Laser Diode*, Springer, Berlin (1997)

[6] W. Van der Stricht, K. Jacobs, I. Moerman, P. Demeester, L. Considine. E.J. Thrush, J.A. Crawley and P. Ruterana, Mat. Res. Soc. Symp. Proc. **482**, 107 (1998)

[7] R.A. Stradling and P.C. Klipstein, *Growth and Characterisation of Semiconductors*, Adam Hilger, Bristol (1990)

[8] http://www.thomasswan.co.uk/ccs_reactor.html

[9] http://www.phys.ksu.edu/area/GaNgroup/

[10] M. Mesrine, N. Grandjean and J. Massies, Appl. Phys. Lett. **72**, 350 (1998)

[11] A. Cho, *Film Deposition by Molecular Beam Techniques*, J. Vac. Sci. Tech. 8, S31-S33 (1978)

[12] F. Calle, F.B. Naranjo, S. Fernández, M.A. Sánchez-García, E. Calleja and E. Muñoz, Phys. Stat. Sol. (a), **192** No. 2, 277 (2002)

[13] http://www.ece.utexas.edu/projects/ece/mrc/groups/street_mbe/mbechapter.html

[14] F.B. Naranjo, M.A. Sánchez-García, F. Calle, E. Calleja, B. Jenichen and K.H. Ploog, Appl. Phys. Lett. **80**, 231 (2002)

[15] John T. Torvik, Jacques I. Pankove, Eleftherios Ilipoulos, Hock M. Ng and Theodore D. Moustakas, Appl. Phys. Lett. **72**, 244 (1998)

[16] N. Grandjean, J. Massies, P. Vennéguès. M. Laügt and M. Leroux, Appl. Phys. Lett. **70**, 643 (1997)

[17] N. Grandjean, J. Massies and M. Leroux, Appl. Phys. Lett. **69**, 2071 (1996)

[18] M.A. Sánchez-García, F.B. Naranjo, J.L. Pau, A. Jiménez, E. Calleja, E. Muñoz, S.I. Molina, A.M. Sánchez, F.J. Pacheco and R. García, Phys. Stat. Sol. (a) **176**, 447 (1999)

[19] M.A. Sánchez-García, E. Calleja, E. Monroy, F.J. Sánchez, E. Calle, E. Muñoz and R. Beresford, J. Crystal Growth **183**, 23 (1998)

[20] Eric Feltin, B. Beaumont, M. Laügt, P. de Mierry, P. Vennéguès, H. Lahrèche, M. Leroux and P. Gibart, Appl. Phys. Lett. **79,** 3230 (2001)

[21] F.B. Naranjo, S. Fernández, M.A. Sánchez-García, F. Calle, E. Calleja, A. Trampert and K.H. Ploog, Mat. Sci. Eng. **B93**, 131 (2002)

[22] O.Madelung, *Semiconductors-Basic Data*, Springer-Verlag, Berlin, 1996

[23] K.P. O'Donnell, R.W. Martin, C. Trager-Cowan, M.E. White, K. Esona. C. Deatcher, P.G. Middleton, K. Jacobs, W. Ven der Stricht, C. Merlet, B. Gil, A. Vantomme and J.F.W. Mosselmans, Mat. Sci. Eng. **B82,** 194 (2001)

[24] V.Yu Davydov, A.A. Klochikhin, V.V. Emtsev, S.V.Ivanov, V.V Vekshin, F. Bechstedt, J. Furthmüller, H. Harima, A.V. Mudryi, A. Hashimoto, A. Yamamoto, J. Aderhold, J. Graul and E.E. Haller, Phys. Stat. Sol. (b), **230**, No.2, R4-R6 (2002)

[25] A. Yamamoto, T.Tanaka, A.G. Bhuiyan, K. Sugita, K. Kasashima, Y. Kimura, A. Hashimoto and V. Yu. Davydov, Talk We-A6.3 at 5th International Conference on Nitride Semiconductors, Nara, Japan (2003)

[26] K.P. O'Donnell, Phys. Stat. Sol. (a) **183,** 117 (2001)

[27] R.W. Martin, P.R. Edwards, K.P. O'Donnell, E.G. MacKay and I.M. Watson, Phys. Stat. Sol. (a) **192,** 117 (2003)

[28] J. Wu, W. Walukiewicz, K.M. Yu, J.W. Ager III, E.E. Haller, Hai Lu and William J. Schaff, Appl. Phys. Lett. **80**, 4741 (2002)

[29] E.V. Kalashnikov and V.I. Nikolaev, MRS Internet J. Nitride Semicond. Res **2**, 3 (1997)

[30] S. Nakamura, Sol. St. Comm. **102**, 237 (1997)

[31] C. Wetzel, T. Takeuchi, S. Yamaguchi, H. Katoh, H. Amano, I. Akasaki, Appl. Phys. Lett**. 73**, 1994 (1998)

[32] B.M. Ashkinadze, I.P. Kretsu, S.L. Pyshkin, S.M. Ryvkin and I.D. Yaroshetskii, Soviet Phys.-Solid State, **No.12**, 2921 (1969)

[33] R.W. Martin, P.G. Middleton, K.P.O'Donnell and W. Van der Stricht, Appl. Phys. Lett. **74**, 263 (1999)

[34] John J. Friel, *X-Ray and Image Analysis in Electron Microscopy*, Princeton Gamma-Tech, Inc. Princeton, United States of America (1995)

[35] http://www.cameca.fr/html/epma_technique.html

[36] D. Amabile, private communication

[37] D.B. Holt and D.C. Joy, *SEM Microcharacterization of Semiconductors*, Academic Press, London (1989)

[38] E. Hecht and A. Zajac, *Optics*, Addison-Wesley Publishing Company, 1982

[39] T.Peng and J.Piprek, Electronics Lett. Online, 19961545 (1996)

[40] M.H.Crawford et al. MRS Internet J. Nitride Semicond. Res. **5S1**, W11.41 (2000)

[41] Y. –H. Cho, G.H. Gainer, A.J. Fischer, J.J. Song, S. Keller, U.K. Mishra and S.P. DenBaars, Appl. Phys.Lett., **73**, 1370 (1998)

[42] K.P. O'Donnell and X. Chen, Appl. Phys. Lett. **58**, 2924 (1991)

[43] K.P. O'Donnell, T. Breitkopf, H. Kalt, W. Van der Straicht, I. Moerman, P. Demeester and P.G. Middleton, Appl. Phys. Lett. **70**, 1843 (1997)

[44] S.D. Baranovskii and A.L. Efros, Sov. Phys. Semicond. **12**, 1328 (1978)

[45] K.P. O'Donnell, R.W. Martin, C. Trager-Cowan, M.E. White, K. Esona, C. Deatcher, P.G. Middleton, K. Jacobs, W. Van der Stricht, C. Marlet, B. Gil, A. Vantomme and J.F.W. Mosselmans, Mat. Sci. Eng. **B82**, 194 (2001)

[46] H. Okumura, S. Yoshida and T. Okahisa, Appl.Phys.Lett., **64**, 2997 (1994)

[47] K.P. O'Donnell, R.W. Martin and P.G. Middleton, Phys.Rev. Lett, **82**, 237 (1999)

[48] K.P. O'Donnell, Phys. Stat. Sol. (a), **189,** 117 (2001)

[49]I.L. Krestnikov, N.N. Ledentsov, A. Hoffmann, D. Bimberg, A.V. Shakarov, W.V. Lundin, A.F. Tsatsul'nikov, A.S. Usikov, Zh.I. Alferov, Yu.G.Musikhin and D.Gertshen, Phys. Rev. **B66**, 155310 (2002)